VEIN AND SKARN FORMATION AT THE CANNINGTON
Ag–Pb–Zn DEPOSIT, NORTHEASTERN AUSTRALIA

Tony J. ROACHE[§], Patrick J. WILLIAMS, Julie M. RICHMOND and Lucy H. CHAPMAN

School of Earth Sciences, James Cook University, Townsville, Queensland 4811, Australia

Abstract

Synchronous deformation and metamorphism at the Cannington Ag–Pb–Zn deposit, in northeastern Australia, involved a phase of Ca and Mn mobilization that accounts for the distribution of pyroxene- and garnet-bearing rocks, which were preferentially overprinted by sulfide mineralization. Garnet composition and its textural association in relation to three generations of planar fabric (S_1 to S_3) show that skarn-related grossular-rich garnet formed in the last garnet-stable event, D_3. The D_3 Cl-rich biotite in the gneiss is intergrown with garnet in veins, and within skarn rocks is continuous along strike with veins of garnet ± pyroxmangite, hedenbergite or amphibole, which indicates a period of anhydrous through to hydrous metasomatism. Compositional maps show that infiltration extended from alteration fronts through fractures, which indicates the high permeability of S_3; these maps and X_{Grt} profiles across skarn–gneiss contacts show that there was large-scale transport of mass by infiltration and varying degrees of hydrodynamic dispersion. Precipitation of oscillatory Ca- and Mn-zoned grossular-rich garnet in veins parallel to veins filled with Cl-rich biotite, in conjunction with the distribution of biotite-filled veins across the deposit, suggest that the mass transfer during D_3 may be responsible for deposit-scale Ca–Mn skarn-like zoning.

Keywords: garnet, zoning, metasomatism, skarn, shear zones, veins, Cannington, Australia.

Sommaire

Une déformation et une recristallisation métamorphique synchrones dans le gisement à Ag–Pb–Zn de Cannington, dans le nord-est de l'Australie, a impliqué une mobilisation de Ca et de Mn qui rend compte de la distribution de roches à pyroxène et grenat, qui sont devenues par la suite les hôtes ciblés d'une minéralisation en sulfures. La composition et l'association texturale du grenat aux trois générations de foliation (S_1 à S_3) montrent que le grenat lié à la formation du skarn, riche en grossulaire, s'est formé lors du dernier épisode de déformation où le grenat était stable, D_3. La biotite de la génération D_3 dans le gneiss, riche en Cl, montre une intercroissance avec le grenat en veines, et dans les roches du skarn, montre une continuité le long de la gneissosité avec des veines à grenat ± pyroxmangite, hedenbergite ou amphibole, indications d'une période de métasomatose anhydre à aqueuse. Des cartes de répartition d'éléments montrent que l'infiltration s'est propagée à partir de fronts d'altération le long de fissures, indication d'une grande perméabilité le long de S_3; ces cartes et les profils de X_{Grt} perpendiculaires aux contacts skarn–gneiss montrent qu'il y a eu transfert important de masse par infiltration et par dispersion hydrodynamique à divers degrés. D'après la précipitation de cristaux de grenat à zonation oscillatoire en Ca et Mn dans des veines parallèles aux veines remplies de biotite riche en chlore, ainsi que la distribution de telles veines de biotite de part et d'autre du gisement, le tranfert de masse au cours de l'événement D_3 aurait été responsable de la zonation en Ca–Mn rappelant un skarn à l'échelle du gisement.

(Traduit par la Rédaction)

Mots-clés: grenat, zonation, métasomatose, skarn, zones de cisaillement, veines, Cannington, Australie.

[§]   *E-mail address*: anthony.roache@goldfields.com.au

INTRODUCTION

Oscillatory zoning in garnet is commonly regarded as representing changes in metamorphic conditions (*e.g.*, Schumacher *et al.* 1999, Willner *et al.* 2000, Yang & Rivers 2001, Garcia-Casco *et al.* 2002); on the other hand, it has been shown through fluid-inclusion studies and mineral equilibria that garnet composition may fluctuate under constant-temperature conditions (Jamtveit *et al.* 1993). Garnet as infill within cavities has been used as evidence to suggest that pulses of hydrothermal fluid and not regional metamorphism were responsible for oscillatory zoning in garnet (Clechenko & Valley 2003), and therefore is an indicator of hydrothermal processes in skarn deposits (Kwak & Tan 1981), and Ca metasomatism in contact-metamorphosed rocks (Stowell *et al.* 1996). In this study, we introduce a new concept to distinguish whether oscillatory zoning in garnet is of metamorphic or hydrothermal origin. Differentiation between several phases of garnet growth on a compositional basis, combined with the association of specific matrix fabrics to each period of garnet growth, and added evidence of oscillatory zoning within a particular generation of fabric, allow discussion of skarn formation relative to the deformation and metamorphic history.

Compositional data and structural interpretation are also used to address the genesis of garnet in the host rocks to the Cannington Ag–Pb–Zn deposit, which is a Broken Hill type of deposit and a world-leading producer of Ag and Pb. The high Mn content of garnet in metamorphosed pelitic rocks surrounding Cannington has been interpreted to either indicate a reconcentration of Mn from sedimentary detritus during metamorphism (Bodon 1998), an addition of fluid or fluids during post-peak-metamorphism metasomatism (Richmond 1994, Chapman & Williams 1998), or a product of a metamorphosed sulfide orebody (Frost *et al*. 2002). Kilometer-scale continuity of horizons bearing high-Mn garnet and gahnite from the nearby Pegmont Pb–Zn deposit (Vaughan & Stanton 1986; Fig. 1), the Broken Hill Pb–Zn–Ag deposit (Walters 1998, Fig. 1), and to the north of Cannington along an north–south-trending lineament with spatially associated Pb–Zn–Ag deposits (Fig. 1), is used to interpret a sedimentary origin for the enrichment in Mn. Sulfides of Ag–Pb–Zn sulfides overprint the pyroxene-, pyroxmangite-, fayalite- and garnet-bearing rocks that are collectively termed Ca–Mn silicate rocks in this paper. The temporal relationship between skarn formation and the development of fabrics in the host rock adds to interpretation of metasomatism in the formation of the Ca–Mn silicate rocks (Chapman & Williams 1998). In this paper, we demonstrate that during skarn formation, structural fabrics were the major conduits for large-scale mass transport, through evidence of oscillatory zoning and the association of Cl-rich minerals, and therefore metasomatism may be responsible for the shaping of mineralized zones at Cannington.

DEPOSIT GEOLOGY

The Cannington Ag–Pb–Zn deposit is situated near the southeastern corner of the Mt Isa Inlier, northwestern Queensland, Australia (Fig. 1). The total resource at Cannington as of June 30, 2001 was estimated to be 40.7 Mt at 545 g/t Ag, 12.2% Pb and 4.3% Zn (Jeffrey 2002). The Mt Isa Inlier, a Proterozoic orogenic belt that has undergone several phases of deformation (*e.g.*, Bell 1983, Betts *et al.* 1998), has a regional metamorphic gradient that increases from the northwest (lower greenschist) to the southeast (upper amphibolite). The Proterozoic upper-amphibolite-facies quartzofeldspathic migmatitic gneiss, and lesser amphibolite and granitic pegmatite that host the Cannington deposit, are overlain by approximately 10–30 m of Cretaceous cover. The gneiss is considered to be part of the Maronan Supergroup (Beardsmore *et al.* 1988), consisting of shallow to deep marine sedimentary and intercalated volcanic rocks with SHRIMP-determined U–Pb zircon ages of deposition in the range 1.68–1.66 Ga (Page & Sun 1998, Giles & Nutman 2003). An amphibolite body, termed the Core Amphibolite, is partially surrounded by the deposit. Peak-metamorphic migmatitic gneiss and anatectic pegmatite have ages between 1.6 and 1.58 Ga based on U–Pb SHRIMP determinations of monazite (Giles & Nutman 2002).

Cannington is divided into Northern and Southern zones by the late Trepell Fault that laterally displaces the Core Amphibolite (Fig. 2a). The zones show marked differences in geology, with alternating cm-scale Ca- and Mn-rich layering in the Northern zone preserving a higher degree of uniformity in garnet, olivine, pyroxene and pyroxenoid along strike. These Ca- and Mn-rich horizons are interpreted as indicating sedimentary layering (Bodon 1998, Walters & Bailey 1998). In contrast, early layering in the Southern zone is typically deformed by discordant fabrics and anatectic, granitic pegmatites. The distribution of the main Ca–Mn silicates in the Southern zone is discernible on the deposit scale, in massive zones up to 100 m wide that locally follow discordant fabrics but have an overall orientation approximately parallel to early layering, rather than as cm-scale bands in the Northern zone. Concentric zones of inner Ca- and Fe-rich hedenbergite – pyroxferroite – garnet and outer Mn-rich pyroxmangite – fayalite – garnet around the Core Amphibolite are broadly similar to those in Zn skarn deposits (Fig. 2b; Chapman & Williams 1998). The concentric zonation is characteristic of the Southern and Northern zones, and transgresses all of the tectonic fabrics that form continuous anastomosing shear-zones past the southern closure of the Core Amphibolite (Roache 2004). Sulfide precipitation accompanied the growth of minerals such as pyrosmalite
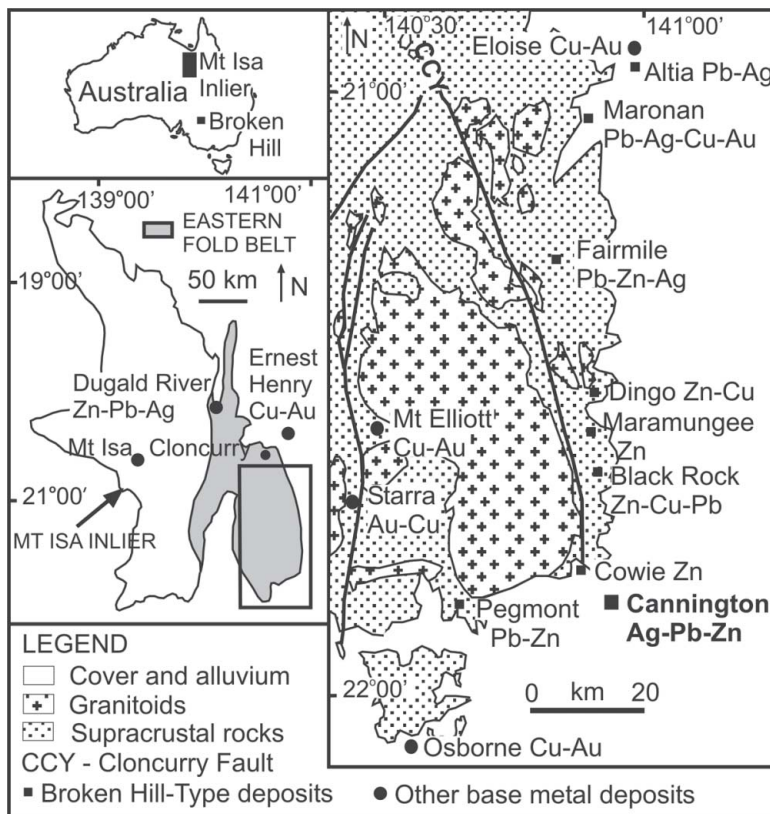
FIG. 1.   The Cannington Ag–Pb–Zn deposit is located near the southeastern corner of the
Eastern Fold Belt, Mt Isa Inlier, Australia. The Maronan Supergroup and Mary Kathleen
Group are condensed into "Supracrustal rocks" [modified from Chapman & Williams
(1998), which was compiled from mapping by the Bureau of Mineral Resources as
Selwyn and Kuridala extended 1:100,000 sheets], and were studied by Beardsmore *et
al.* (1988), and Williams & Phillips (1992).

and chlorite, and overprinted the Ca–Mn silicate rocks surrounding the Core Amphibolite. Sphalerite- and galena-dominated orebodies are located in zones of predominantly hedenbergite and pyroxmangite, respectively (Chapman & Williams 1998). Mineralization closely follows the contacts of the Core Amphibolite, with most of the mineralization contained in the Southern zone, down-plunge of the predominantly banded, comparatively low-grade mineralization of the Northern zone (Fig. 2a).

Garnet compositions within the Southern Zone have been documented in a number of studies (Mark 1993, Chapman 1993, Richmond 1994, Richmond *et al.* 1996). In this study, garnet growth is divided into three distinct phases related to the D_1, D_2 and D_3 events. Event D_1 represents a northwest-directed thrusting during peak metamorphism and migmatization, and was followed by east-directed extension and the development of D_2 silli-manite–biotite shear zones (Roache 2004). Progressive shearing during D_2 is responsible for most of the small-scale asymmetries that were previously interpreted as parasitic folds to a synform at the southern closure of the Core Amphibolite (Gray 1992, Bodon 1998, Giles 2000). Event D_3 is characterized by conjugate fabrics, further alteration of the gneiss, and a garnet–pyroxene assemblage that overprints S_1 and S_2 (Fig. 2a). Gray (1992) proposed that two sets of folds with easterly and southeasterly plunging fold-axes deformed the rocks in the deposit following D_2 (of this study), whereas Giles (2000) recognized only one set of north-trending open folds following D_2. Neither Gray (1992) nor Giles (2000) recognized fabrics axial planar to post-D_2 folds.
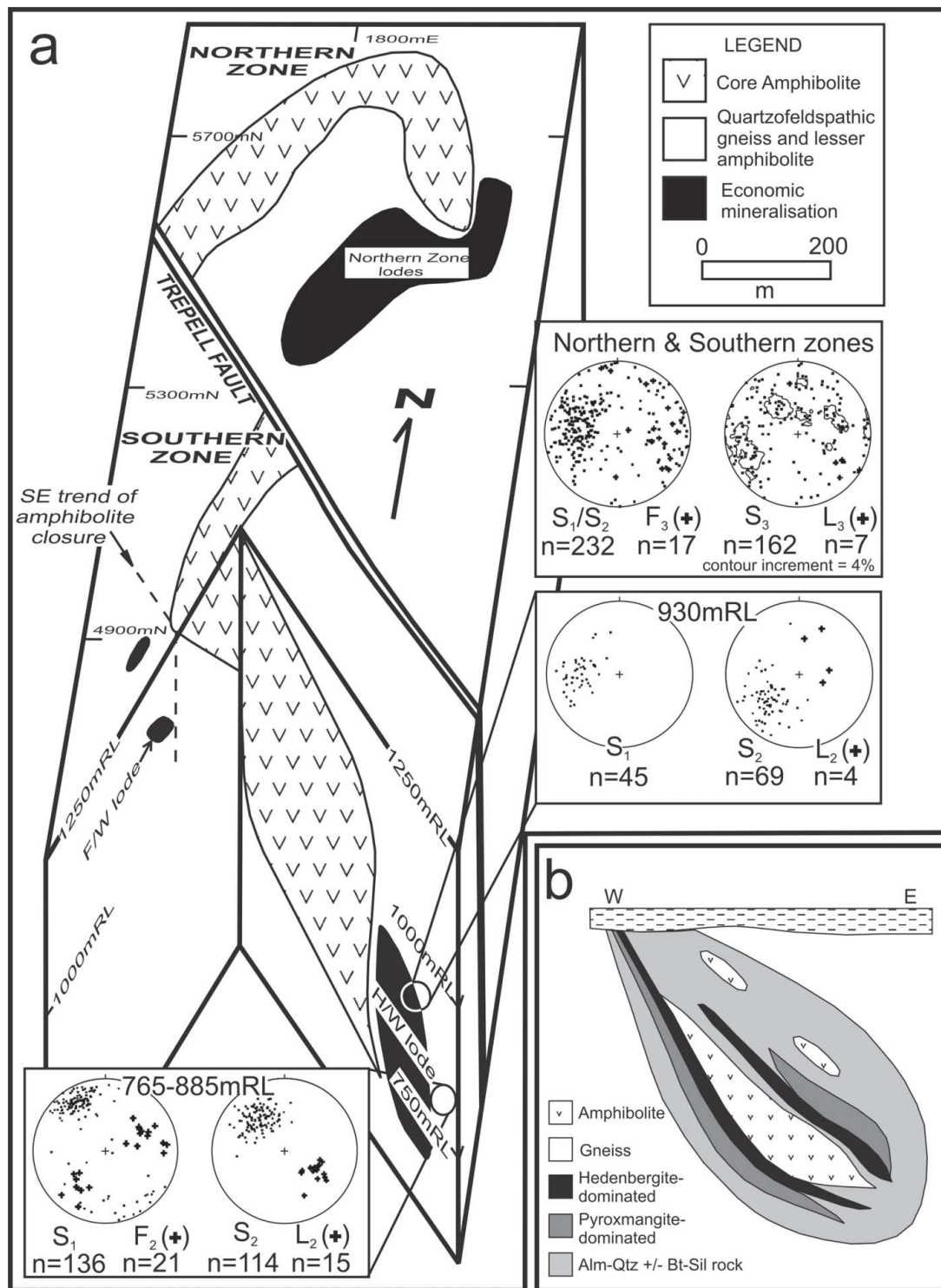
ANALYTICAL METHODS

Mineral assemblages that are texturally affiliated with S_1 to S_3, and collected from representative parts of the underground workings at the Southern zone, were selected from a series of normal thin sections for the preparation of polished thin sections ready for compositional analysis. Two drill-core samples containing a Ca–Mn silicate – gneiss contact were selected for traverses of garnet perpendicular to the orientation of the contact, which covered up to three polished sections end to end. Chemical compositions of garnet, plagioclase, biotite and muscovite were determined by energy-dispersion spectrometry (EDS) on the JXA–840A electron microprobe at James Cook University. An acceleration potential of 15 kV, a beam current of 10 nA and 40 s counting time were used. Corrections were applied with the program Zaph (Moran Scientific), which was used to calculate wt% oxides and elements. The following standards for EDS analyses were used: wollastonite (Ca), plagioclase (Al), albite (Na), kaersutite (Ti), almandine (Fe), pyrope (Mg), sanidine (K), bustamite (Mn) and tugtupite (Cl), and were supplied by Astimex. An average result of three spot analyses represents each data point in this paper. Garnet compositions taken from Mark (1993) have been included with the new results, and are assigned to a D_1, D_2, or D_3 origin through re-interpretation of their texture and matrix associations. Mineral abbreviations are after Kretz (1983), and representative compositions of garnet, plagioclase, biotite and muscovite are given in Table 1.

FIG. 2. Deposit geometry and host rocks. a) Schematic block-diagram of the Cannington Ag–Pb–Zn deposit. The retrograde Trepell Fault laterally displaced the Core Amphibolite and divides the deposit into Northern and Southern zones. Small-scale observations and structural mapping of D_1 fabrics suggest that the Core Amphibolite has a sigmoidal asymmetry in a vertical southeasterly trending section. Lower-hemisphere stereographic projections of S_1 and S_2, L_2 and F_2 from the Southern zone show shear-zone development and evidence of associated immature sheath-type folds. S_1 and S_2 were observed to be deformed by multiply-oriented S_3 from numerous parts of the Northern and Southern zones. The Southern zone contains most of the mineralization within the hanging-wall (H/W) and footwall (F/W) lodes, and is generally more massive and metal-enriched than the predominantly banded mineralization in the Northern Zone (modified from Giles 2000, Roache 2004). b) Generalized cross-section through the Southern zone, with spatial distribution between Ca–Mn silicate rocks (hedenbergite–pyroxmangite zones), Mn-enriched gneiss (Alm – Qtz ± Bt – Sil), amphibolite and gneiss, adapted from section 4800 mN, compiled from Chapman (1993), Mark (1993), Strain (1993), Roche (1994), and Roache (2004).

Three compositional maps of garnet were made with the JXA8200 electron microprobe at James Cook University. All maps are 500×500 pixels and constructed with a wavelength-dispersion spectrometer with 3 μm step size and probe diameter, 150 nA probe current, and 70 ms dwell time. The computer program IMAGEJ was used to extract the single-element image files from the dataset, with consistent use of a single plugin (image editing file), multi.lut, for color generation.

TYPES OF GARNET

D_1-related garnet

The D_1 assemblages include biotite + K-feldspar + quartz + garnet migmatitic gneiss, K-feldspar + quartz + garnet pegmatite and amphibolite with margins altered to biotite + garnet + ilmenite + plagioclase (An$_{20–34}$). A gneissic layering and biotite + garnet + ilmenite schistosity, S_1, are parallel to margins of the Core Amphibolite (Roache 2004, Fig. 2). The D_1-related garnet shows

TABLE 1. REPRESENTATIVE COMPOSITIONS OF GARNET, PLAGIOCLASE, BIOTITE AND MUSCOVITE IN METAPELITES AND AMPHIBOLITE FROM THE SOUTHERN ZONE OF THE CANNINGTON DEPOSIT, AUSTRALIA

	1	2	3	4	5	6	7	8	9	10
SiO$_2$ wt.%	38.34	37.64	36.29	36.66	36.88	36.71	36.54	66.84	32.48	44.53
TiO$_2$								0.00	3.19	0.80
Al$_2$O$_3$	20.82	20.39	20.92	20.77	20.85	20.71	19.76	19.62	17.51	34.18
Fe$_2$O$_3$*	0.00	0.00	0.00	0.00	0.91	1.59	3.12			
FeO	28.90	27.63	36.14	36.23	29.11	28.74	19.44	0.00	30.22	1.70
MnO	5.22	5.49	3.51	3.80	6.21	7.22	7.26			
MgO	2.41	2.60	2.21	1.93	1.34	1.22	1.03	0.25	1.72	0.59
CaO	5.66	5.72	0.34	0.24	5.06	3.99	11.76	0.47	0.00	0.00
Na$_2$O								11.08	0.00	0.44
K$_2$O								0.00	9.75	11.50
Cl								0.00	0.91	0.00
total	101.34	99.47	99.41	99.63	100.36	100.19	98.91	98.27	95.77	93.73
Si apfu	6.06	6.05	5.94	5.99	5.94	5.94	5.92	11.86	5.26	6.09
Ti								0.00	0.39	0.08
Al	3.88	3.86	4.04	4.00	3.96	3.95	3.77	4.10	3.34	5.50
Fe^{3+}*	0.00	0.00	0.00	0.00	0.11	0.19	0.38			
Fe^{2+}	3.82	3.71	4.95	4.95	3.92	3.89	2.63	0.00	4.09	0.19
Mn	0.70	0.75	0.49	0.53	0.85	0.99	1.00			
Mg	0.57	0.62	0.54	0.47	0.32	0.29	0.25	0.07	0.41	0.12
Ca	0.96	0.99	0.06	0.04	0.87	0.69	2.04	0.09	0.00	0.00
Na								3.81	0.00	0.12
K								0.00	2.01	2.00
Cl								0.00	0.25	0.00
total	15.97	15.98	16.01	15.98	15.97	15.95	15.98	19.94	15.76	14.11
Pyrope	9.4	10.3	9.0	7.9	5.4	5.0	4.2			
Andradite*	0.0	0.0	0.0	0.0	2.7	4.7	9.3			
Almandine	63.2	61.2	82.0	82.7	65.8	66.3	44.5			
Spessartine	11.6	12.3	8.1	8.8	14.2	16.9	16.8			
Grossular	15.9	16.2	1.0	0.7	11.9	7.1	25.2			

Column headings: 1: garnet pps111, D_1, core, amphibolite; 2: garnet pps111, D_1, rim, amphibolite; 3: garnet ps151, D_2, core; 4: garnet ps151, D_2, rim; 5: garnet ps158, D_3, core, matrix; 6: garnet ps158, D_3, rim, matrix; 7: garnet ps158, D_3, rim, vein; 8 plagioclase ps159, D_2; 9 biotite pps127, D_3; 10 muscovite pps127, D_3. *In garnet compositions, the proportion of Fe$_2$O$_3$, Fe^{3+} and the andradite component is estimated from charge-balance considerations. Proportion of garnet components in mol. %.
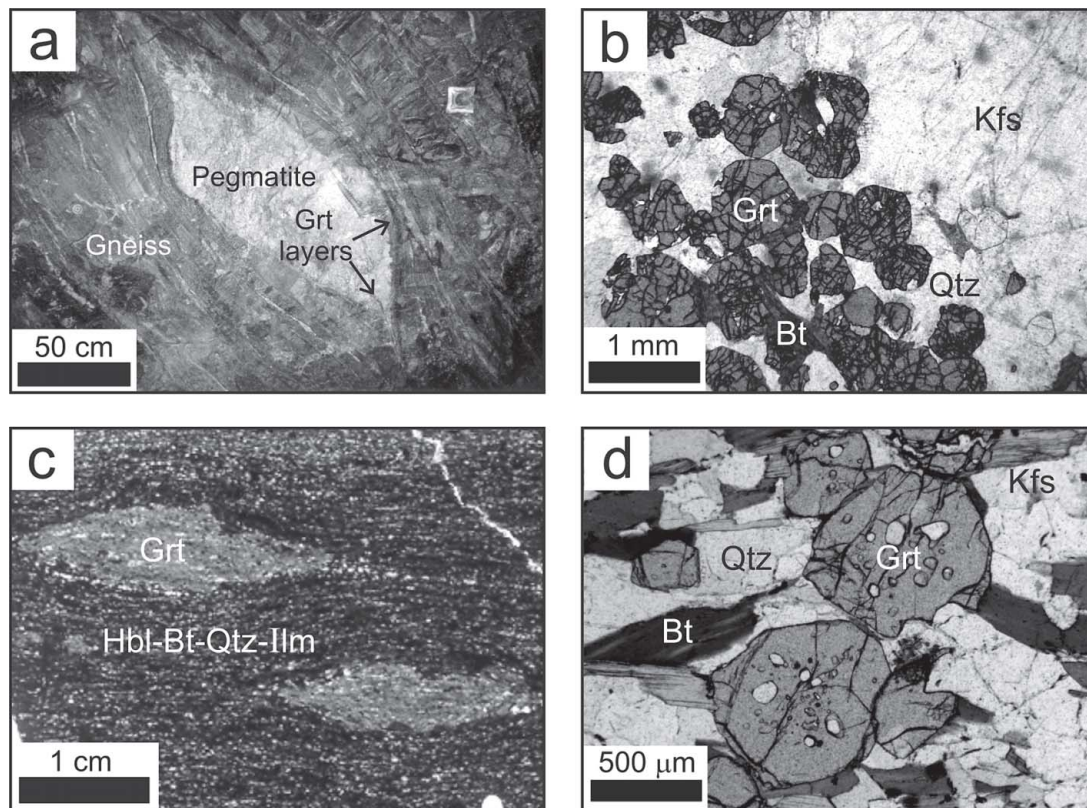
FIG. 3.   D$_1$-related garnet and textures. a) Underground exposure of a near-sygmoidal pegmatite body viewed in an orientation (NNE) that is oblique to the D$_1$ extension direction as derived from lineation data. Garnet-rich layers have developed at the contact between pegmatite and gneiss (4654mN, 1836mE, 933mRL). b) Plane-polarized light photomicrograph of garnet (Grt) layers within pegmatite that is in contact with gneiss, showing the costable biotite (Bt), K-feldspar (Kfs) and quartz (Qtz) (Sample 24, 4892mN, 2026.5mE, 930mRL). c) Thin section of D$_1$-related garnet within amphibolite, viewed in a section parallel to the elongation of biotite and maximum elongation of garnet. Garnet coexists with hornblende (Hbl), biotite (Bt), quartz (Qtz) and ilmenite (Ilm) (Sample 57, 4459mN, 1820.5mE, 885.7mRL). d) Plane-polarized light photomicrograph of fine-grained D$_1$-related garnet (Grt) in gneiss, showing garnet grains with a characteristically inclusion-rich core. Garnet is intergrown with biotite (Bt) and quartz (Qtz) (Sample 99, 4548.5mN, 1915.5mE, 858mRL).

evidence of synchroneity with S$_1$ through the alignment of individual grains or layers of garnet within pegmatite (Fig. 3a). Pegmatite bodies are commonly enriched in garnet; layers of fine-grained garnet (Fig. 3b) are parallel to aplitic margin of the pegmatite, and to S$_1$ in the adjacent gneiss (Roache 2004, Fig. 5). Geological modeling of drill-core logs and underground geological maps shows a higher concentration of pegmatite within the Southern zone compared to the Northern zone (pers. commun., S. Jeffrey, 2002). Centimeter-scale porphyroblasts of garnet within altered amphibolite are aligned parallel to a biotite-elongation lineation, L$_1$, and have trails of biotite + quartz + ilmenite inclusions that are continuous with the matrix (Fig. 3c). Lineation L$_1$ is approximately parallel to the plunge and trend of the

Core Amphibolite, 47° toward 140°, which was determined from the position of the southern Core Amphibolite closure (Fig. 2a). Unlike D$_1$-related garnet within altered amphibolite, D$_1$-related garnet in the gneiss is fine-grained, 0.5–1.0 mm, equidimensional, and typically contains a quartz-inclusion-rich core and inclusion-free rim (Fig. 3d).

The D$_1$-related garnet within altered amphibolite is unzoned. Garnet within the gneiss has a lower Ca and Mg content than in amphibolite, and typically has a Mg-depleted rim that is consistent with retrograde zoning (Grant & Weiblen 1971). The growth zoning from core to rim defines a clustered trend oriented away from the pyrope vertex, and it corresponds to an increase in Fe and decrease in Mg (Fig. 4).
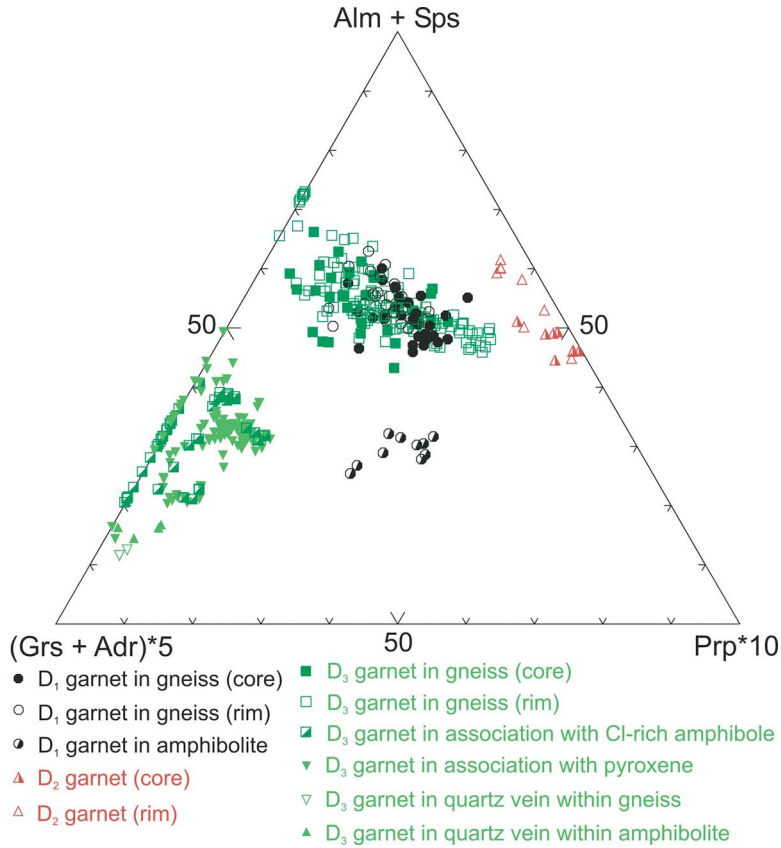
FIG. 4. Plot of D_1-, D_2-, and D_3-related garnet compositions. Each vertex is equal to 100%. The data are scaled to enable differentiation among D_1, D_2 and D_3 garnet within the gneiss, which would not be possible on an unscaled triangular diagram trimmed to a quadrilateral. The D_1-related garnet in amphibolite is unzoned. The scatter of D_1 and D_2 garnet compositions in the gneiss is controlled by depletion of Mg from core to rim. The D_3-related garnet within the gneiss is not zoned, but the spread of compositions is mainly controlled by changes in coexisting assemblages of minerals in the matrix , which forms an overall trend that is oblique to the D_1-related garnet within the gneiss. The cluster of D_3 grossular-rich garnet defines a trend that is controlled by varying concentrations of grossular and spessartine where garnet is spatially associated with amphibolite – apatite – hedenbergite and pyroxmangite – fayalite rocks, respectively. In all, 54 D_1 analyses were made from 16 samples, 10 D_2 analyses from four samples and 178 D_3 analyses from 18 samples for the current study. In addition, 21 D_1 compositions from three samples and 203 D_3 compositions from 17 samples were taken from P. Williams, J. Richmond and L. Chapman (unpublished). Six D_2 compositions from one sample were taken from Mark (1993). Seven D_3 compositions were taken from Chapman (1993).

D_2-related garnet

A schistosity S_2, involving the assemblage sillimanite + muscovite + biotite + garnet + albite ($An_{2–9}$) ± quartz ± corundum ± gahnite, deformed and modified S_1. Biotite is commonly intergrown with sillimanite within D_2 shear zones that anastomose around coarse D_1-related K-feldspar, with the margins of the latter replaced by albite (Fig. 5a). Within the K-feldspar, biotite grains and elongate trails of albite have formed parallel to the adjacent biotite and sillimanite. The D_2-related garnet may be up to several centimeters in size, infrequently with sillimanite inclusions that are continuous with muscovite-altered sillimanite in the matrix (Fig. 5b), and increases in abundance within zones of intense S_2 where the garnet is foliation-parallel (Fig. 5c).
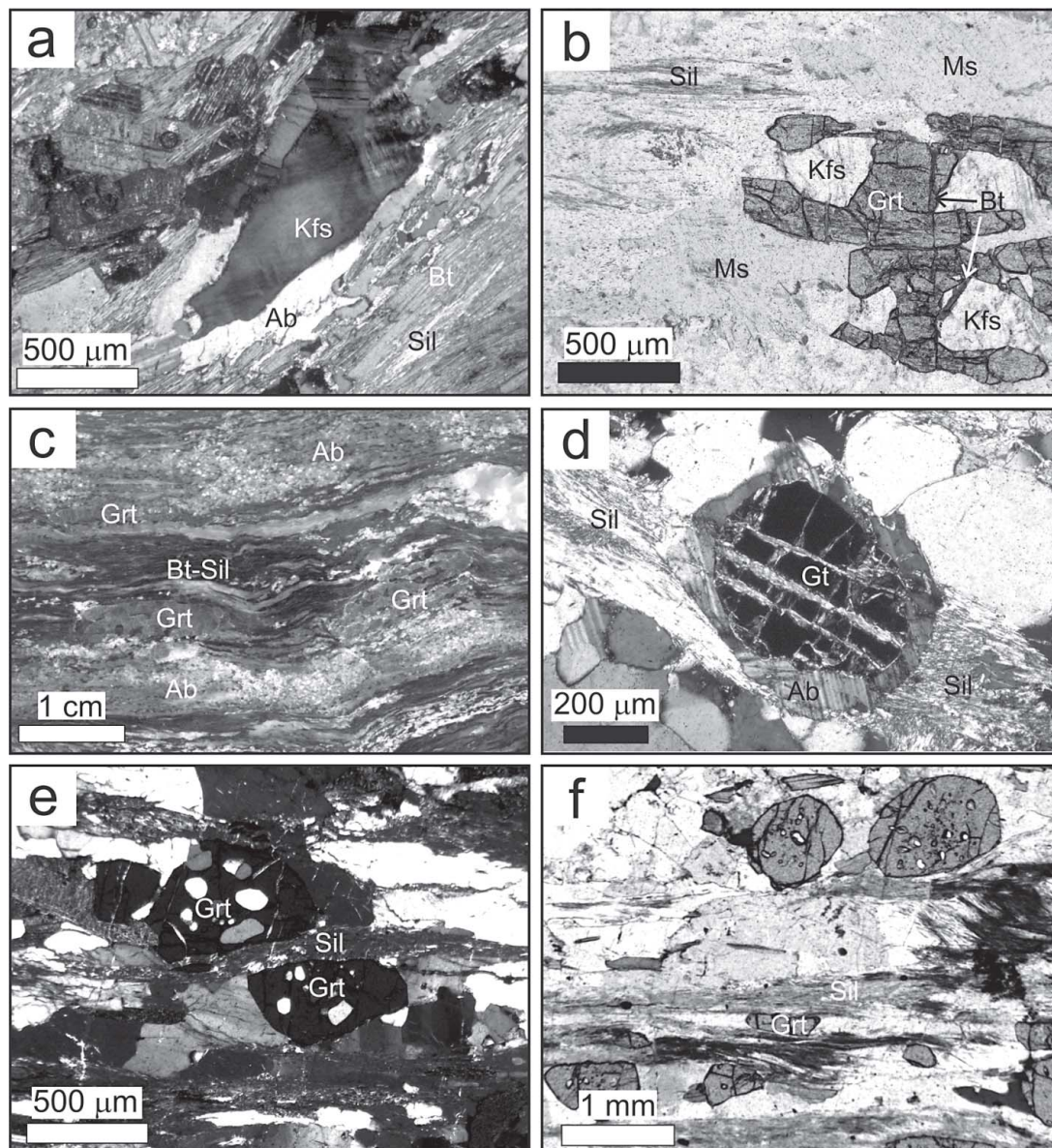
FIG. 5. D_2 textures. a) Cross-polarized light photomicrograph of D_1-related K-feldspar (Kfs) with rims replaced by albite (Ab) and enveloping biotite (Bt) and sillimanite (Sil) (Sample 33, 4431mN, 1825mE, 886mRL). b) Plane-polarized light photomicrograph of D_2-related garnet (Grt) intergrown with sillimanite (Sil) that was replaced by K-feldspar (Kfs) and biotite (Bt). The predominantly sillimanite-bearing matrix was replaced by muscovite (Ms) (CAD041 508.4m). c) Hand specimen of D_2 garnet (Gt), with growth parallel to biotite–sillimanite schist (Bt–Sil) and albitized D_1 leucosomes (Ab) (Sample 33, 4431mN, 1825mE, 886mRL). d) Cross-polarized light photomicrograph of D_2 garnet (Gt) rimmed by albite (Ab) and penecontemporaneous with a sillimanite-lined shear-zone (Sil). Note that the garnet is fractured and infilled with late chlorite (CAD061 575.3m). e) Cross-polarized light photomicrograph of D_1 garnet (Grt) displaced by D_2 sillimanite-lined shear-zones (Sil) (Sample 99, 4548.5mN, 1915.5mE, 858mRL). f) Plane-polarized light photomicrograph of the change in axial ratio of D_1 garnet (Grt) from outside (top) to inside (bottom) of sillimanite-lined shear-zones (Sil) (Sample 99, 4548.5mN, 1915.5mE, 858mRL).

The distribution of albite mimics that of D_2-related garnet within intense S_2. Albite commonly rims garnet and appears to postdate sillimanite (Fig. 5d), but albite is in turn overprinted by sillimanite in adjacent grains.

The D_2-related garnet is distinguished from D_1-related garnet because the latter is overprinted and dissolved along sillimanite shear-zones. Deformation of D_1 garnet is shown through the displacement of single grains (Fig. 5e), and is supported by a preferred orientation where garnet is enveloped by sillimanite (Fig. 5f). Axial dimensions of 200 grains of D_1 garnet measured parallel and perpendicular to the orientation of sillimanite-lined shear zones reveal an axial ratio of $1.1 \pm 0.15:1$ where sillimanite is not in contact with garnet, and $2.1 \pm 0.76:1$ where sillimanite envelops garnet (Fig. 6).

The D_2-related garnet is lower in the grossular component than D_1-related garnet, and displays a consistent retrograde zonation away from the pyrope vertex on the composition diagram (Fig. 4).

D_3-related garnet

Combinations of garnet + K-feldspar + biotite + muscovite + quartz + apatite are representative of a fabric, S_3, that deformed and modified S_1 and S_2. Fabric S_3 commonly defines sharp boundaries between gneiss and Ca–Mn silicate rocks, in which it is axial planar to folds in the gneiss, and undeformed layering within the Ca–Mn silicate rocks is parallel to the westerly dipping limb of folded S_1 (Fig. 7a). Layering in the Ca–Mn silicate rocks does not commonly preserve evidence of a tectonic fabric that would distinguish it from a pre-S_1 compositional layering. Fabric S_3 in the gneiss typically displays a quartz-depleted matrix, particularly surrounding biotite + garnet + muscovite foliations (Fig. 7b). Garnet is aligned along the muscovite cleavage that is also parallel to the overall trend of the foliation (Fig. 7c), and is not due to a static replacement of sillimanite as in other cases (Fig. 5b). Muscovite that is interpreted to grow late in D_2 (Roache 2004) can be differentiated from D_3-related muscovite if biotite coexists with muscovite in the rock (*cf*. Evans & Guidotti 1966). In rocks with D_2-related textures, higher values of Mg / total Fe for coexisting muscovite and biotite compared to D_3-related muscovite and biotite suggest that the metamorphic temperature decreased from D_2 to D_3 (Fig. 7d). D_3-related K-feldspar is differentiated from coarse-grained D_1-related K-feldspar by its association with fine-grained garnet that infilled fractured D_1-related pegmatite (Fig. 7e). Coarse-grained, euhedral apatite is
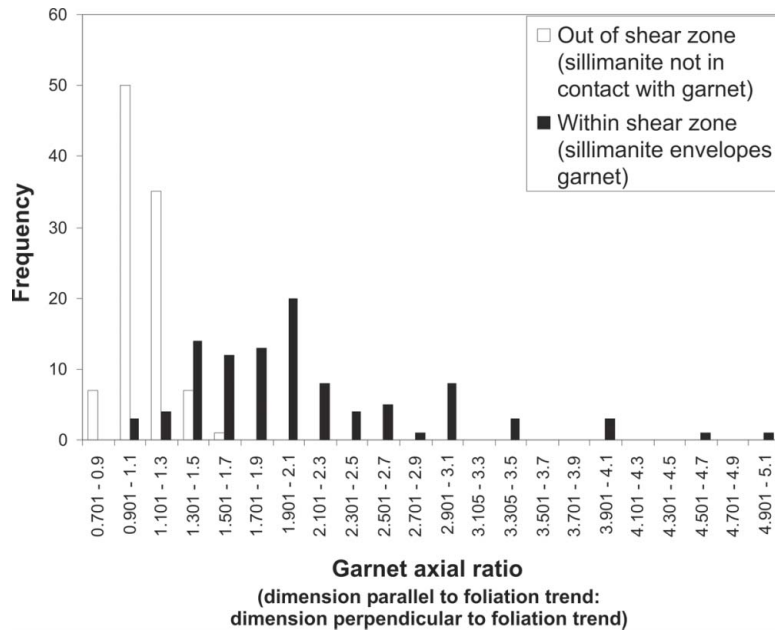

FIG. 6. Histogram showing the anisotropy of D_1-related garnet in sample 99, in which linear dimensions were measured parallel and perpendicular to the S_2 sillimanite foliation trend and expressed as an axial ratio. Garnet enveloped by sillimanite (within the shear zone) has a higher mean and standard deviation than garnet that is not enveloped by sillimanite (out of the shear zone). The axial ratio of the garnet is divided into 0.2 intervals.
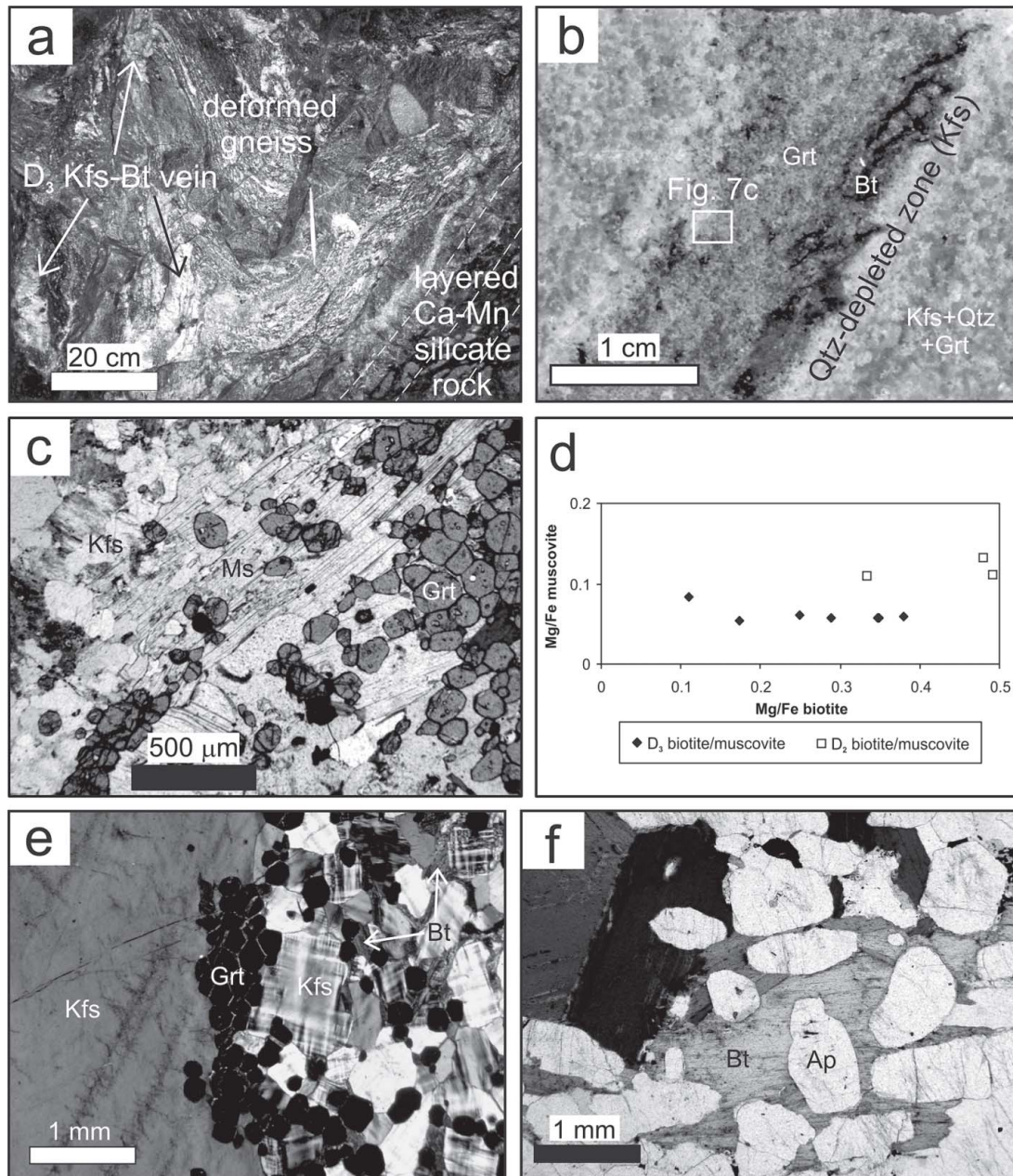
FIG. 7.   D₃ textures and composition. a) Underground exposure of D₃ Kfs–Bt veins that deform S₁ within the gneiss into paral-
lelism with undeformed layering within Ca–Mn silicate rock, shown as dashed lines (right) (looking NNE; 4623mN, 1850mE,
933.5mRL). b) Hand specimen of S₃ delineated as segregated Kfs–Grt–Bt±Ms zones within a gneiss that shows predomi-
nantly massive Kfs–Qtz–Grt alteration associated with D₃ (CAD045 204.3m). c) Plane-polarized light photomicrograph of a
section of b), displaying a synchronous relationship between garnet (Grt) that grew parallel to muscovite (Ms) cleavage. The
latter is dominantly oriented parallel to the trend of S₃ (CAD045 204.3m). d) Plot of Mg / total Fe for coexisting micas,
showing the difference between D₂ and D₃ muscovite. e) Cross-polarized light photomicrograph of D₃-related garnet (Grt),
K-feldspar (Kfs) and biotite (Bt) that replaces D₁-related K-feldspar (left of image) (CAD203 304.82m). f) Plane-polarized
light photomicrograph of intergrown D₃-related biotite (Bt) and euhedral apatite (Ap) (Sample 98, 4788mN, 2048.5mE,
729mRL).

only found within the gneiss in association with D_3-related textures and assemblages (Fig. 7f).

The D_3-related biotite contains anomalous concentrations of Cl, and forms within a schistosity with a measurable elongation-lineation of biotite in the gneiss, and veins that are found within the gneiss and the Ca–Mn silicate rocks. The D_3-related biotite can be distinguished from D_1- and D_2-related biotite by a higher Cl content, combined with lower Mg/(Mg + Fe), although there is some variation in the Cl content of biotite on the scale of a thin section (Fig. 8a). A Cl content below detection levels within biotite included within D_1-related garnet is in contrast to biotite in the adjacent matrix, which contains 1.0 wt% Cl (Roache 2004, Fig. 6c). As a general rule, D_3-related biotite defining the schistosity and that in veins have >1.5 wt% Cl, which is a consistent association within gneiss, amphibolite and Ca–Mn silicate rocks. The veins are commonly contemporaneous with the Cl-rich biotite schistosity, although veins predominantly cross-cut garnet or K-feldspar grains within D_3-modified gneiss (Fig. 8b). Veins that are filled by K-feldspar ± biotite ± quartz or garnet ± biotite ± quartz share the characteristics of biotite-filled veins, and are all considered to have formed late during D_3. Cl-rich biotite ± garnet-filled veins are discordant to the main rock fabrics in the gneiss, namely relict S_1 and S_2, and can be traced along strike to within Ca–Mn silicate rocks, in which Cl-rich ferropargasite, biotite, grossular-rich almandine and pyroxmangite coexist. The rocks surrounding biotite ± garnet or pyroxmangite or hedenbergite or ferropargasite veins are generally depleted in biotite and K-feldspar or plagioclase, but contain a recrystallized quartz matrix with minor biotite aligned parallel to the relict foliation (Fig. 9a). Hedenbergite, Cl-rich biotite and ferropargasite also coexist in some Ca–Mn silicate rocks (Fig. 9b), although ferropargasite replaces hedenbergite in some examples. Rare allanite forms veins parallel to garnet-filled veins that extend from Ca–Mn silicate rocks into the gneiss. The axial planar relationship of allanite and garnet to folded, relict S_1–S_2 implies that both types of vein were contemporaneous. Allanite is spatially and texturally associated with ferropargasite, biotite, scapolite and tourmaline in veins and shears, particularly within amphibolite, but the ferropargasite in the above assemblage is texturally similar to the ferropargasite that replaces hedenbergite and garnet in the Ca–Mn silicate rocks. The Cl content of ferropargasite that replaces hedenbergite and garnet, and that is also costable with scapolite, is higher than in ferropargasite that is costable with hedenbergite and garnet (Fig. 9c). Thus, the paragenesis of biotite and ferropargasite in the different rock-types may be constrained by Cl content as well as by texture. Intergrown hedenbergite or pyroxmangite + biotite + garnet are considered to be a D_3 assemblage on the basis of a common textural and structural association with the D_3 assemblage within the gneiss, and ferropargasite and allanite are considered to be stable during and immediately after the D_3 event.

The D_3-related garnet within the host gneiss is partly distinguished from D_1-related garnet by having a component of andradite, particularly where grains are euhedral (Fig. 9d). The linear trend of D_3-related garnet hosted by gneiss is not defined by retrograde zoning as
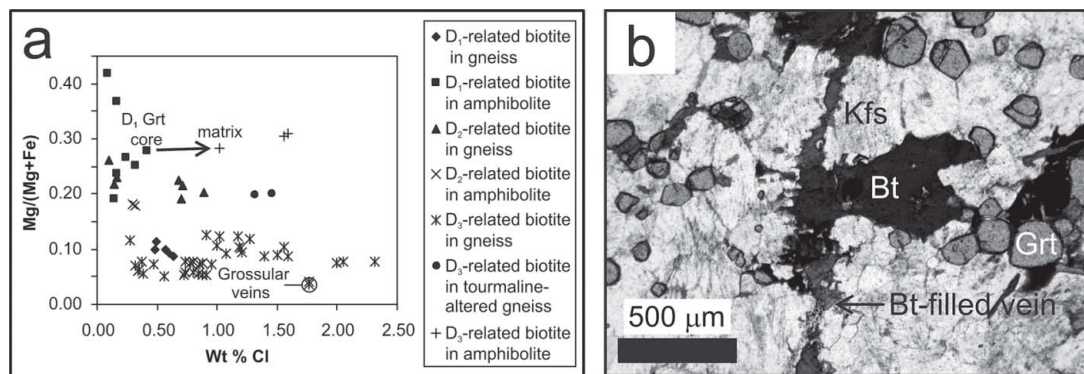

FIG. 8. Texture and composition of D_3-related biotite. a) Plot of Mg/(Mg + Fe) against wt% Cl for D_1-, D_2- and D_3-related biotite. The Cl content of biotite within gneiss and amphibolite increases from D_1 and D_2 to D_3. An increase in the Cl content of biotite as inclusions within D_1-related garnet (D_1 Grt core), to biotite in the surrounding matrix (matrix), suggests that alteration of D_1- and D_2-related biotite may explain the variability in Cl on the scale of a thin section. Biotite within grossular-rich veins (Grossular veins) and S_3 within the gneiss consistently have a Cl content greater than 1.5 wt%. Nine compositions of biotite from four samples were taken from Mark (1993). b) Plane-polarized photomicrograph of a late D_3-related biotite-filled vein (vertical), cross-cutting Kfs and a Bt–Grt foliation (horizontal). The biotite within the vein and foliation show synchronous crystallization (CAD203 305m).
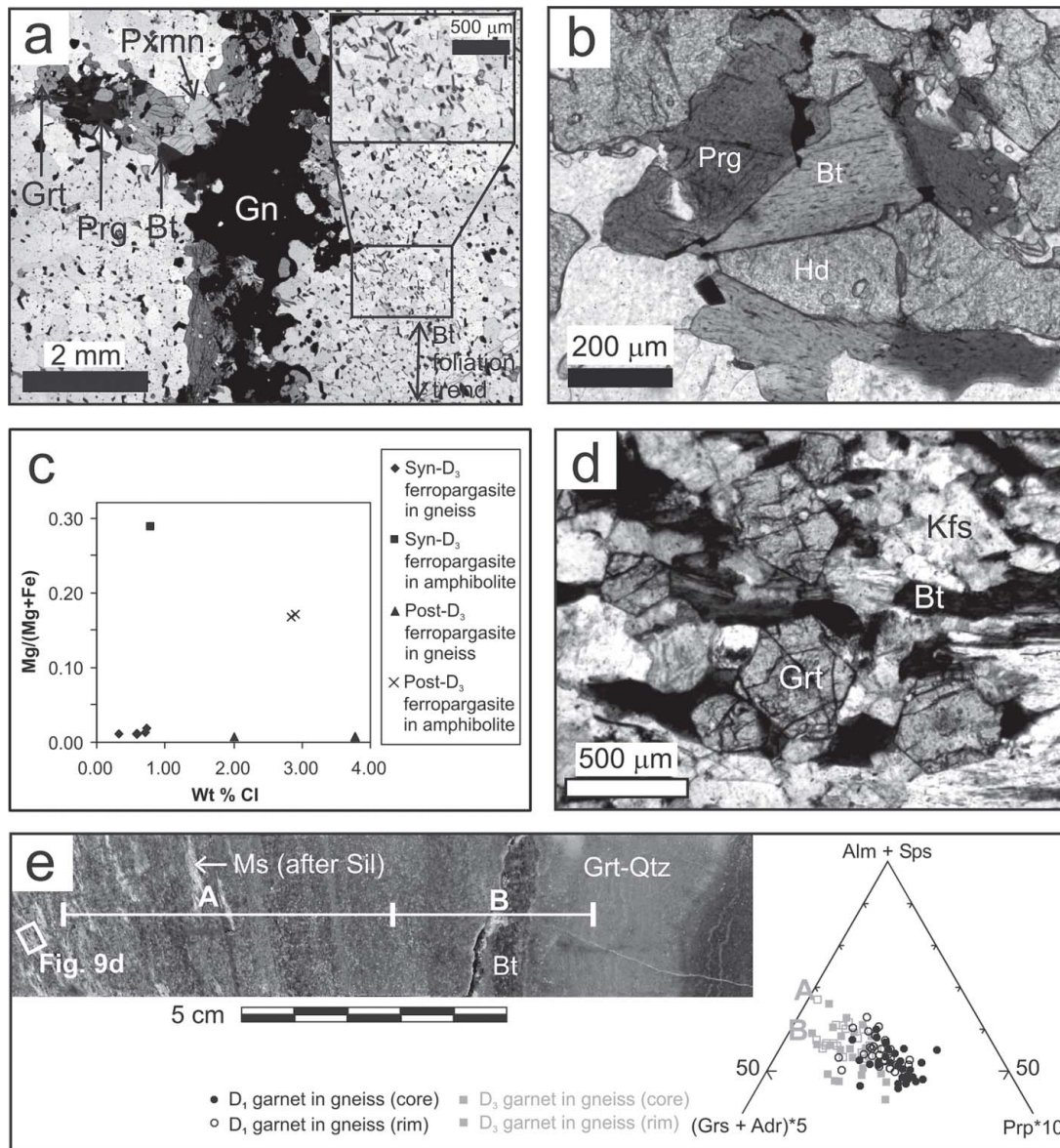
FIG. 9.   Texture and composition of D₃ minerals. a) Plane-polarized light photomicrograph of a vein containing grossular-rich garnet (Grt), ferropargasite (Prg), biotite (Bt) and pyroxmangite (Px) (left of image) within Ca–Mn silicate rock. The veins are discordant to layering of the same mineralogy and aligned biotite grains (inset) that define a 2-mm-wide foliation (CAD061 542.73m). b) Plane-polarized light photomicrograph of intergrown ferropargasite (Prg), biotite (Bt), and hedenbergite (Hd) within Ca–Mn silicate rock (sample 69, 4513mN, 1870mE, 858.5mRL). c) Plot of Mg/(Mg + Fe) against wt% Cl for syn- and post D₃-related ferropargasite in gneiss and amphibolite. The Cl content of ferropargasite increases from syn- to post-D₃. d) Plane-polarized light photomicrograph of coexisting euhedral garnet (Grt), biotite (Bt) and K-feldspar (Kfs) from the inset in e) (CAD066 174.4m). e) A garnet compositional traverse is delineated on a hand specimen of gneiss, and is separated into sections, A and B. A compositional plot of garnet shows that the change in mineralogy from muscovite (Ms) to alternating zones of biotite (Bt) and Grt–Qtz relates to a change in the composition of garnet from trend A to trend B (CAD066 174.4m).

in the case of D_1-related garnet, but by a change in the composition of garnet within mineralogically different units in the gneiss. In Figure 9e, compositions of garnet within muscovite + biotite + garnet define a compositional trend A, whereas within garnet + biotite + quartz, garnet composition is defined by trend B. Trends A and B are oblique to the compositional trend of D_1-related garnet and, combined with garnet compositions from other D_3 assemblages, emphasize that obliquity (Fig. 4). Ca–Mn silicate rocks contain a grossular-rich garnet that is D_3 in origin but is compositionally distinct from D_3-related almandine in the gneiss (Fig. 4). Grossular-rich garnet in association with apatite and within quartz veins in amphibolite is relatively enriched in Ca, whereas that in association with pyroxmangite and Mn-rich fayalite

is relatively Mn-rich, thus defining the linear trend of grossular-rich garnet.

D_3 compositional traverses and maps

At the contact between the gneiss and Ca–Mn silicate rocks, there are two types of textural relationships. The first is an example of a sharp transition in sample 42224(ii), which was collected by Richmond (1994) from drill core. The gneiss is altered to a muscovite + K-feldspar + garnet schist with euhedral almandine that forms interlocking clusters. Clinozoisite + muscovite ± biotite defines a cm-wide zone that separates the gneiss from a grossular-rich garnet, quartz and Cl-rich biotite (Fig. 10a). The latter unit represents the Ca–Mn silicate
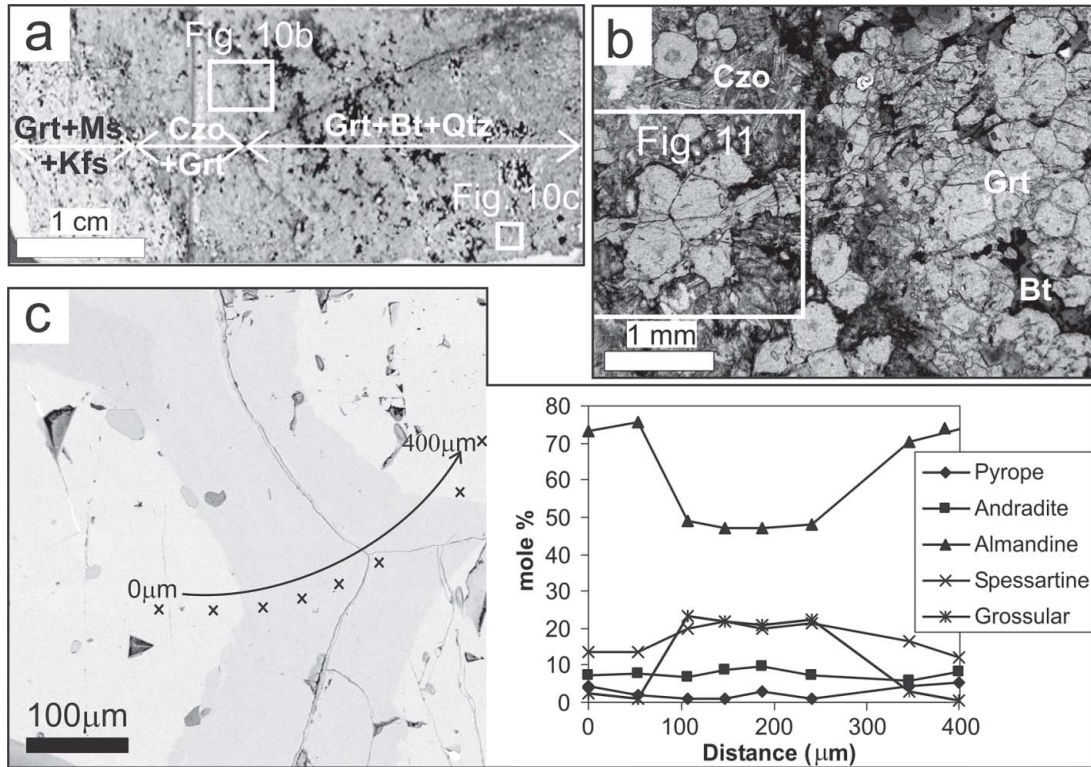

FIG. 10.   Garnet composition and texture in sample 42224(ii) from drillhole CAD045, 245.75m (4600N). a) Polished thin section of sample 42224(ii). Clinozoisite, euhedral garnet and grossular-rich garnet-filled veins (Czo + Grt) delineate the contact between grossular-rich garnet, relict euhedral garnet, biotite and quartz (Grt + Bt + Qtz), and euhedral garnet, muscovite and K-feldspar (Grt + Ms + Kfs), that represent Ca–Mn silicate rock and gneiss, respectively. Note that b) and c) are shown as insets. b) Plane-polarized light photomicrograph of interlocking euhedral garnet rimmed by grossular-rich garnet from the inset in a). A grossular-rich vein extends from the margin of the massive Grt + Bt zone and preferentially formed around a small cluster of euhedral grains of garnet on the left. Clinozoisite is the dominant matrix mineral surrounding the garnet-filled fractures. The inset represents the compositional map in Figure 11. c) Plot of mole % garnet against distance across sharp compositional contacts within the Ca–Mn silicate rock (inset in a). The back-scattered electron image shows the traverse across a junction of interlocking euhedral grains of garnet where individual rims have been overgrown by grossular-rich garnet.

rock that changes to dominantly quartz, then becomes hedenbergite-dominated over an interval of approximately five meters, and is 15 m into the hangingwall of a 150-m-wide unit of Ca–Mn silicate rock that hosts the main sulfide mineralization. The orientation of the host rock, clinozoisite and grossular-rich garnet contacts is parallel to the foliation in the host. The grossular-rich garnet and Cl-rich biotite veins are discordant to the dominant layering and extend into the clinozoisite + muscovite ± biotite zone, where grossular-rich garnet preferentially replaces euhedral almandine compared to the matrix minerals (Fig. 10b). Sharp, micro-scale compositional changes are associated with the replacement of almandine rims by grossular-rich garnet (Fig. 10c). A compositional map shows fracturing of almandine and infill by a grossular-rich garnet vein (Fig. 11). The sharp compositional change in the Ca image best displays the fracturing. Preserved triple-point junctions of euhedral almandine shows that original almandine rims have been replaced by grossular-rich garnet. Enrichment in Mn and depletion in Mg and Fe are associated with vein fracturing. The grossular-rich vein shows oscillatory zoning of Ca and Mn (Fig. 11).

The second style of transition is in relation to veins of grossular-rich garnet that are both concordant and discordant to earlier layering in the gneiss. A chemical traverse across one such vein in samples ps157–159 in the footwall to the main Ca–Mn silicate rocks reveals a gradual change in garnet composition over a centimeter scale, from grossular-rich in the vein to almandine in the gneiss (Fig. 12a). Almandine garnet in this example is texturally related to D_2, as described above (Fig. 5b), with D_3-related K-feldspar + biotite that replaced garnet, and D_3-related muscovite that replaced sillimanite. Garnet compositions at analytical points 1–15 (Fig. 12a) are shown in Figure 12b. Plagioclase is a part of the D_2 assemblage and, along with garnet, is characterized by decreasing Ca away from the vein. The Ca content of plagioclase and garnet is approximately linear with respect to distance (Fig. 12c). The analytical gap for plagioclase between points 8 and 13 represents a K-feldspar layer, with plagioclase found on either side. Individual grains of garnet in the gneiss also display compositional variation. Garnet grains proximal to the vein have a Ca- and Mn-enriched rim (Fig. 13a), *i.e.*, grains at analytical points 6–11 on the garnet-composition plot (Fig. 12b). Calcium enrichment of garnet rims is particularly characteristic where plagioclase is in direct contact with garnet. A change in garnet zonation between points 11 and 12 is marked by a change in matrix mineralogy from biotite + K-feldspar + muscovite, to muscovite + plagioclase ± sillimanite + corundum, and a geochemical transition is marked by an abrupt increase in almandine and a decrease in grossular and spessartine components (Fig. 12a). Garnet grains from points 12–15 are weakly zoned with respect to Mn, and have a Mg-depleted rim that corresponds to Mn enrichment (Fig. 13b). Garnet at points 12–15 plot along an extension of the D_2 garnet
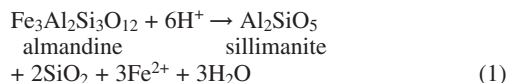
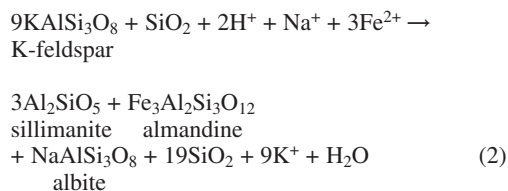trend (Fig. 12b), and lack the Ca zonation of garnet at points 6–11 (Fig. 13a).

DISCUSSION

D_1 and D_2 metasomatism

High concentrations of Mn in D_1-related garnet (12 mole % spessartine) are not expected nor regionally developed in amphibolite with low concentrations of Mn (Smith 1999); therefore, Mn may have been derived from the surrounding gneiss and concentrated at contacts with amphibolite. A spatial association between D_1-related garnet and Mn-bearing ilmenite has been suggested as an indication of pre-D_1 metasomatism (Smith 1999), but could also be interpreted as syn-D_1. Partial melting during migmatization may have influenced the metasomatic distribution of Mn, as shown in the concentric enrichment of garnet around bodies of pegmatite (Fig. 3a). Similarities between the prolate shape and linear orientation of the Core Amphibolite, meter-scale pegmatite bodies and centimeter-scale garnet, all of which are enveloped by S_1, suggest that the concentration of Mn observed on a small scale may also operate on the scale of the Core Amphibolite. Thrust shear-zone formation during D_1 may have localized Mn-rich fluid surrounding the Core Amphibolite, as observed in the concentration of Mn-enriched garnet at the underground exposure to hand-specimen scale.

Base-ion leaching (*cf.* Vernon 1979) involving sillimanite at Cannington has been proposed by Mark *et al.* (1998) and Giles (2000). Textures indicate that D_1-related garnet was resorbed during formation of sillimanite-lined shear zones (Fig. 5f; *cf.* Mark 1993), involving the reaction:

$$Fe_3Al_2Si_3O_{12} + 6H^+ \rightarrow Al_2SiO_5$$
$$\text{almandine} \qquad\qquad \text{sillimanite}$$
$$+ 2SiO_2 + 3Fe^{2+} + 3H_2O \qquad\qquad (1)$$

Replacement of K-feldspar and growth of D_2-related garnet and albite within sillimanite-lined shear- zones (Fig. 5d) are proposed *via* the reaction:

$$9KAlSi_3O_8 + SiO_2 + 2H^+ + Na^+ + 3Fe^{2+} \rightarrow$$
$$\text{K-feldspar}$$

$$3Al_2SiO_5 + Fe_3Al_2Si_3O_{12}$$
$$\text{sillimanite} \quad \text{almandine}$$
$$+ NaAlSi_3O_8 + 19SiO_2 + 9K^+ + H_2O \qquad (2)$$
$$\quad \text{albite}$$

Coexistence of D_2-related garnet, albite and sillimanite may be associated with the breakdown of anorthite to give grossular + sillimanite + quartz, but calculation of pressure using the GASP geobarometer is not possible since anorthite and grossular contents are too low (Todd 1998, Holdaway 2001). Nevertheless, albite rim-
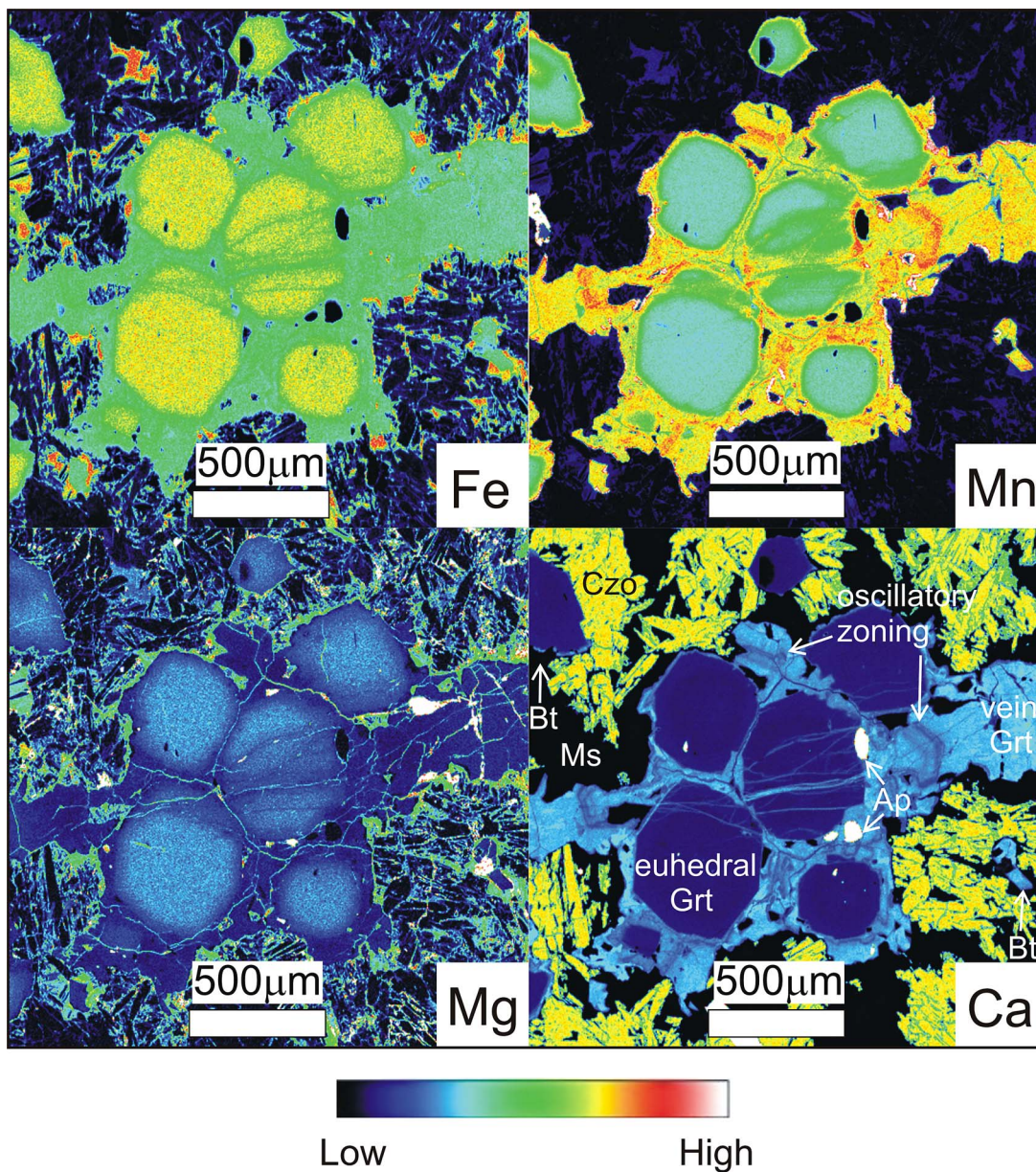
FIG. 11.   Fe, Mg, Mn and Ca X-ray maps in sample 42224(ii). Warmer colors indicate higher concentrations. The area is outlined by the inset in Figure 10b, and shows a grossular-rich vein intersecting a cluster of euhedral grains of garnet. Minor D_3-related Cl-rich biotite (Bt) is preserved in the matrix, but most of the D_3 matrix contains clinozoisite (Czo) and retrograde fine-grained muscovite (Ms).

ming grossular-poor garnet may indicate a lowering of metamorphic pressure during D_2. Roache (2004) previously suggested that grossular-rich garnet may be a product of D_2, growing simultaneously in rocks that do not contain sillimanite, but in this study, we suggest a D_3 origin for growth of pyroxene and garnet within the Ca–Mn silicate rocks.

D_3 metasomatism

A textural and geometrical link between D_3 assemblages in the gneiss and Ca–Mn silicate rock may point to a contemporaneous origin, but their contrasting composition needs explanation. Compositional traverses
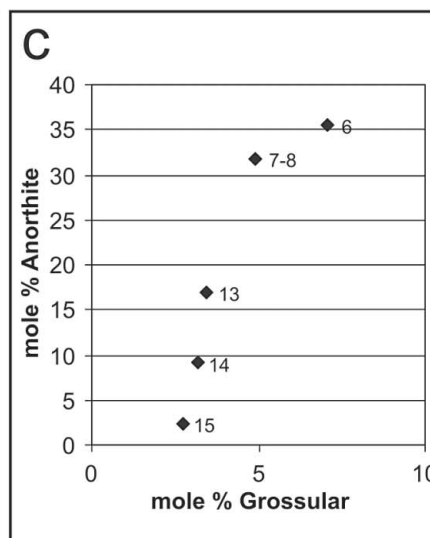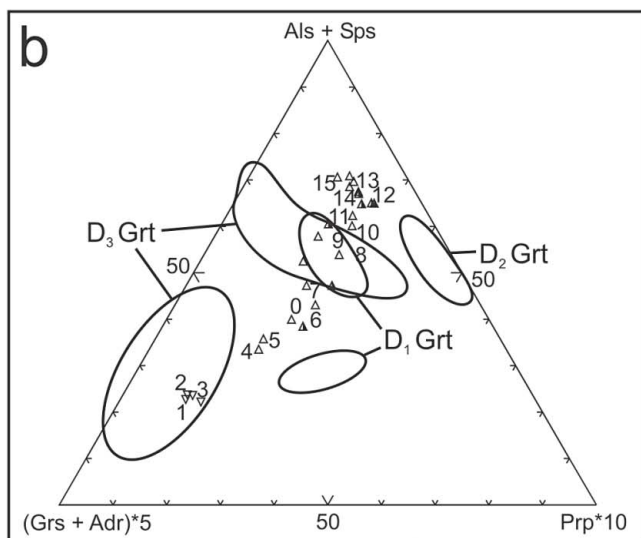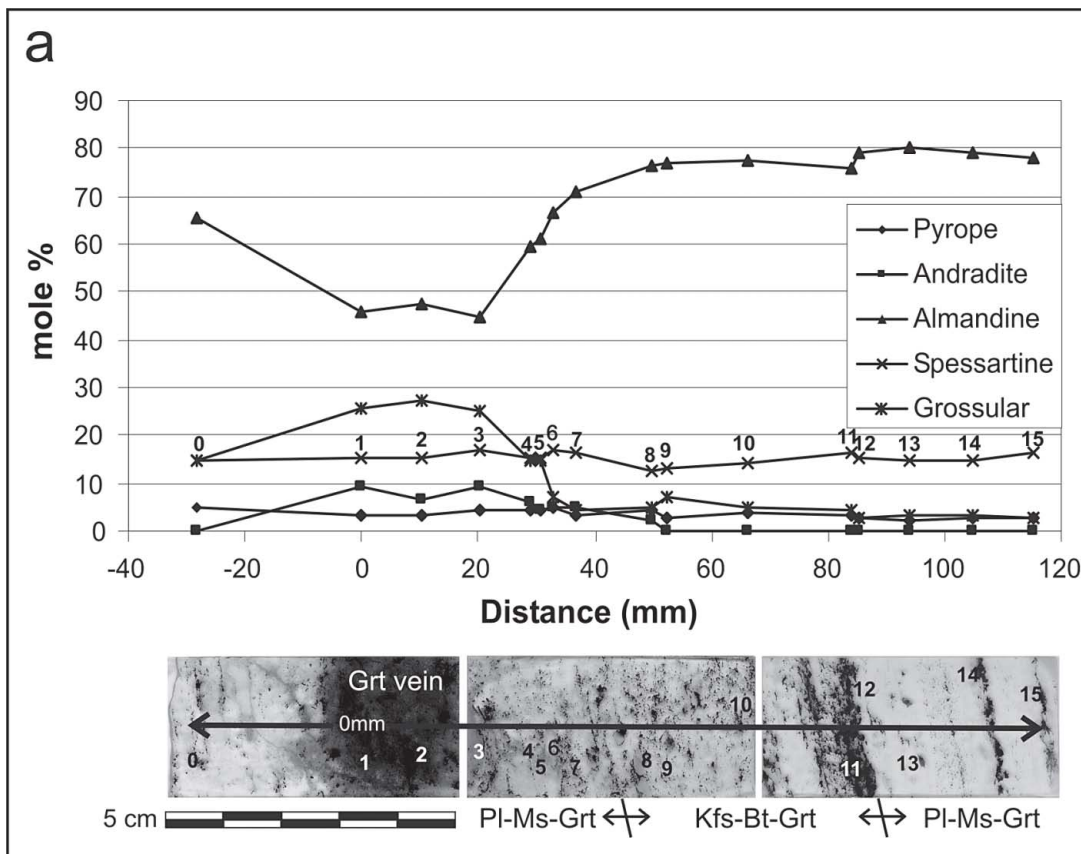
across contacts between gneiss and Ca–Mn silicate rock aid in that interpretation.

A plot of garnet composition against distance for sample 42224(ii) suggests the possibility of fluid infiltration (Fig. 10c), which is supported by the clear overprinting of grossular-rich domains upon almandine. Modification of early D_3-related almandine involves a straight substitution of Fe for Ca, and is shown in the simplified exchange-type reaction:

$$Fe_3Al_2Si_3O_{12} + 3Ca^{2+} \rightarrow Ca_3Al_2Si_3O_{12} + 3Fe^{2+} \quad (3)$$

almandine   grossular
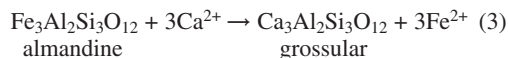
Veins filled with Cl-rich biotite intergrown with grossular-rich garnet provide a petrographic link to similar veining in the host gneiss that is considered to have formed late in D_3. Preservation of early D_3-related euhedral garnet on the right of Figure 10a shows that the infiltration front advanced to the left of the image, and therefore the (muscovite + K-feldspar + garnet)-modified gneiss was overprinted by Ca–Mn silicate rock. Minor intracrystalline diffusion was responsible for the redistribution of Fe and Mg within fractured early D_3-related garnet, but it is the sharp compositional change with distance that supports advection through late-D_3 garnet-filled veins (Fig. 11). The oscillatory zoning of Ca and Mn shows that Mn may also be a major constituent in reaction 3, as a partial substitution of Ca. Fluctuating parameters that may include activity, flow rate, P and T control the distribution of Ca and Mn.

The vein containing the grossular-rich garnet in gneiss samples ps157–159 is interpreted to have resulted from advection as in sample 42224(ii), but the X_{Grt} against distance profile is more typical of hydrodynamic dispersion during infiltration (e.g., Bowman et al. 1994). Proximal to the vein, Ca alteration of D_2-related garnet is greatest where plagioclase is in contact with garnet (Fig. 13a), which corresponds to a decrease X_{Ca} in gros-

sular and anorthite contents away from the vein. Well-developed enrichment of Mn and depletion in Mg in garnet rims close to the garnet vein (Fig. 13a) compared to garnet further away from the vein (Fig. 13b) suggest that a spatial association with metasomatic veining as in sample 42224(ii) may be responsible for zoning rather than retrograde metamorphism. The sharp boundary in the X_{Grt} against distance profile between point 11 and 12 may represent the extent of a D_3 alteration front, or equally may be represented by a previous mineralogical boundary (Fig. 12a). Weak D_3 alteration beyond point 11 is recognizable through a linear correlation of decreasing X_{Ca} between grossular and anorthite contents (Fig. 12c).
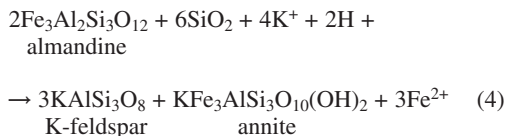
An estimate of peak metamorphic conditions at 650–690°C and 4–6 kbar has been derived from garnet–biotite geothermometry, dehydration reactions and plots of assemblages on phase diagrams (Mark et al. 1998), and is considered to be contemporaneous with D_1 of this study. Metamorphism during D_2 was still within the stability field of sillimanite, but only a few quantitative P–T estimates could be calculated from D_3 equilibria. Two P–T estimates from the spreadsheet GPT (Reche & Martinez 1996), and one from a calculation of average P–T from AX–THERMOCALC (Powell et al. 1998) were the only calculations possible from the range of D_3 assemblages within the gneiss. Two of the estimates are a comparison of GPT and AX–THERMOCALC methods from sample ps157–159. The elevated concentration of Ca in plagioclase at the periphery of the vein filled with grossular-rich garnet (Fig. 12) made the calculations possible, in combination with coexisting garnet – biotite –muscovite. All three estimates plotted in the sillimanite stability field on a phase diagram, which does not comply with petrological evidence, as D_3 assemblages replace sillimanite (Fig. 14). Electron-microprobe data for seven examples of D_3 assemblage within the gneiss were used to calculate temperature using the 20 garnet–biotite pairs in GPT. The GPT-derived estimates of temperature consistently overlapped the stability field of sillimanite, with estimates for each sample averaging between 700 and 800°C. An estimate of temperature by similar means within the Ca–Mn silicate rock in sample 42224(ii) yielded an average temperature 400°C higher than that estimated for the D_3 assemblages in the gneiss. Giles (2000) cited evidence of rare kyanite within gneiss assemblages comparable to D_3 of this study; therefore, quantitative estimates of temperature using GPT and THERMOCALC are up to 200°C too high. A temperature estimate of 450–550°C is derived from coexisting hedenbergite, amphibole, garnet and quartz, combined with fluid-inclusion data from the same assemblage within the Ca–Mn silicate rocks (Pollard et al., in prep.), and may reflect a closer approximation of temperature during D_3. We consider that the D_3 assemblages within the gneiss and Ca–Mn silicate rocks were synchronous with skarn formation, and thus are not amenable to quantitative P–T estimates from

FIG. 12. Garnet composition in sample ps157–159 between a D_3 grossular-rich garnet vein, and a layered Kfs–Bt–Grt and Pl–Ms–Gt gneiss (CAD041, 508.3–508.5m, 5000N). a) A plot of mole % of certain elements in the garnet rim against distance shows a gradational decrease in Ca and increase in Fe away from the grossular-rich garnet vein. Sample points 0–15 coincide with photographed thin sections that show the traverse across a garnet vein (dark domain) and surrounding gneiss that was modified to sillimanite–plagioclase schist. b) Triangular plot showing compositional fields of D_1-, D_2- and D_3-related garnet (data from Fig. 4) overlapped by compositions from the ps157–159 traverse that show a transition from grossular-rich garnet to altered Mg-depleted D_2-related garnet. c) Plot of mole % anorthite against mole % grossular. Each point is marked with its location from a).
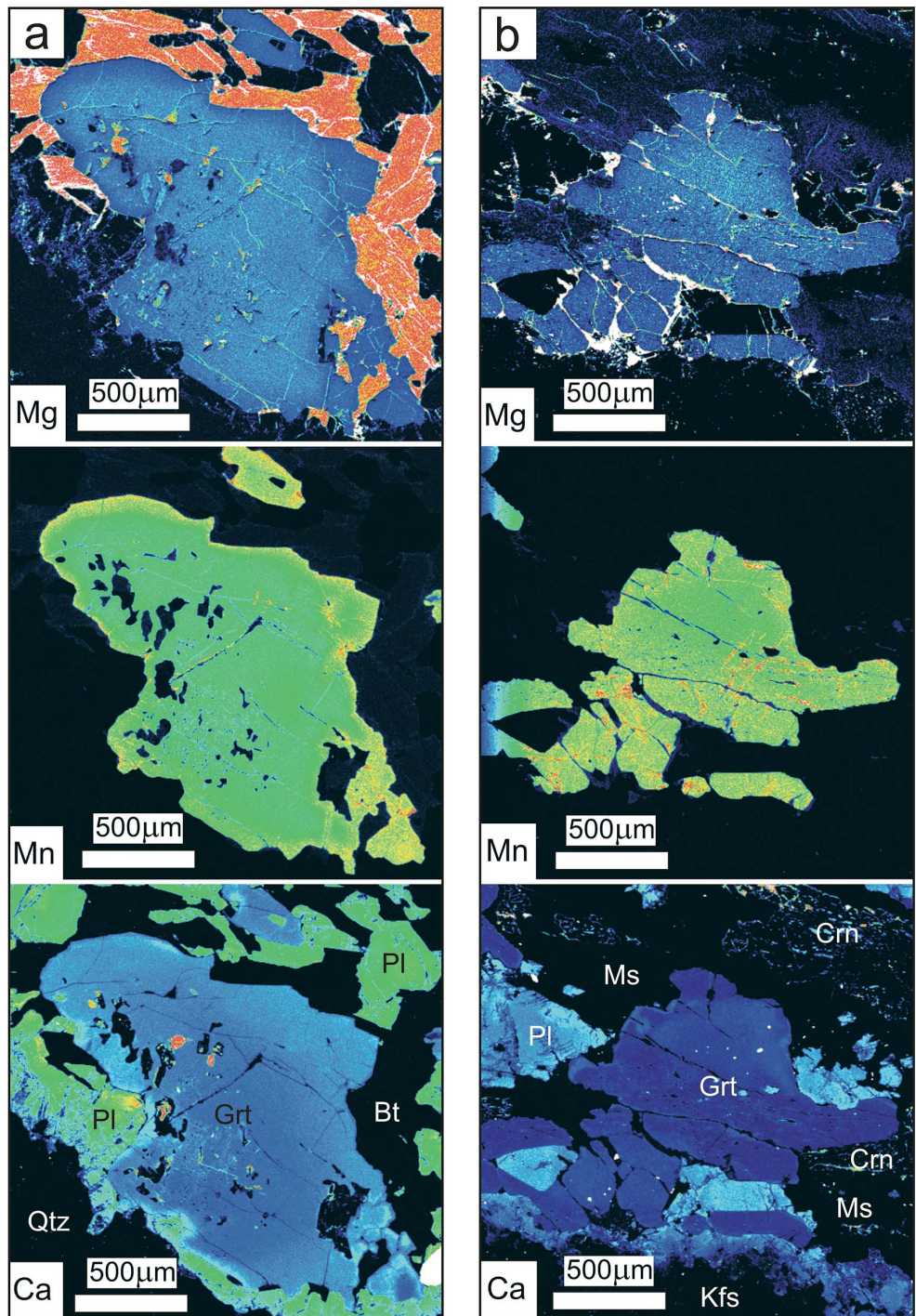
equilibria calculated from regional metamorphic rocks. The poorly constrained P and T for D_3 assemblages reflect the wide range of fluid conditions in which the rocks could have formed; for example, the andradite content of D_3-related garnet indicates the introduction of an oxidizing fluid and the necessity to involve fluid phases other than H_2O. Discussion of multiple fluid phases will be deferred to a later paper.

High concentrations of Ca, Mn and Fe in premineralization fluid-inclusions from Cannington are considered to be derived from phases such as hedenbergite, garnet and pyroxenoids during high-temperature metasomatism (Williams *et al*. 1999). High concentrations of Cl and K from the same inclusions are interpreted to contribute to a range of mineral resorption and growth reactions during D_3, particularly within the gneiss that surrounds the deposit. The D_3-related biotite and ferropargasite accommodated elevated concentrations of Cl in their crystal structure as a result of interaction with a hypersaline fluid, with Fe and K cations interpreted to contribute to the resorption and growth of D_2 and D_3 phases, respectively, in order to explain the metasomatic nature of the D_3 mineral texture within the gneiss. The assemblage D_2-related garnet + quartz was replaced by K-feldspar + biotite (Fig. 5b) according to reaction:

$$2Fe_3Al_2Si_3O_{12} + 6SiO_2 + 4K^+ + 2H +$$
almandine

$$\rightarrow 3KAlSi_3O_8 + KFe_3AlSi_3O_{10}(OH)_2 + 3Fe^{2+} \quad (4)$$
K-feldspar   annite

The replacement of coarse K-feldspar by intergrown K-feldspar + garnet + biotite (Fig. 7e) is shown by the reaction:

$$4KAlSi_3O_8 + 6Fe^{2+} + 2H^+$$
K-feldspar

$$\rightarrow [KAlSi_3O_8 + Fe_3Al_2Si_3O_{12}$$
K-feldspar   almandine
$$+ KFe_3AlSi_3O_{10}(OH)_2] + 3Si^{4+} + 2K^+ \quad (5)$$
annite

Veins that cross-cut and fracture the gneiss and S_1–S_2 indicate high permeabilities during D_3; in consideration of the X_{Grt} profiles in Figures 10c and 12a, combined with reactions 4 and 5, these veins show that there is large-scale transport of mass by advection and varying degrees of hydrodynamic dispersion. Micro-scale veining in sample 42224(ii) displays how fluid is transferred between broader, massive zones of garnet alteration through the fracturing of pre-existing minerals (Fig. 11). Meter-scale layering of pyroxene or pyroxenoid and garnet (Fig. 7a) is commonly interlinked by D_3-related veins (Fig. 9b), and is considered to have formed through infiltration and replacement of S_1 and S_2 within the gneiss, as in sample 42224(ii). Centimeter-scale grossular-rich veins (*e.g.*, sample ps157–159) that are tens of meters away from broad zones of Ca–Mn silicate rocks show that fluid transfer occurred on a deposit scale, and the spatial and temporal association with biotite ± garnet ± K-feldspar ± quartz-filled veins and shears (*e.g.*, Figs. 7a, 8a) that extend beyond the deposit may indicate that the latter were a regionally extensive conduit for D_3 fluid.

Oscillatory zoning in grossular-rich garnet veins (Fig. 11) demonstrates that Ca–Mn distribution in pyroxene–garnet rocks may be explained by metasomatic flow through structurally controlled conduits, and not only as a remnant of sedimentary processes. The latter conclusion agrees with the interpretations of Bodon
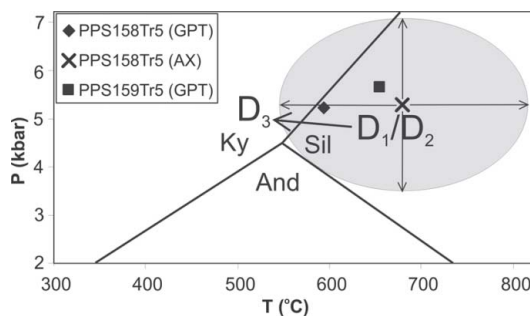
FIG. 14. Phase diagram with P–T estimates of D_1, D_2 and D_3, shown in relation to the aluminosilicate triple point of Larson & Sharp (2003). Estimates derived from GPT and AX–THERMOCALC were found to have considerable error, and in association with Grt–Bt geothermometry overestimated the temperature of D_3. Fluid-inclusion and petrographic data constrain the temperature of D_3 to be outside the stability field of sillimanite.
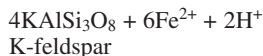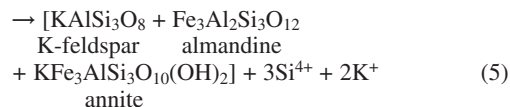
FIG. 13. Mg, Mn and Ca X-ray maps in sample ps157–159. Warmer colors indicate higher concentrations. a) X-ray maps taken from point 7 of the traverse, within polished thin section ps158. Biotite (Bt), plagioclase (Pl) and quartz (Qtz) are the dominant matrix minerals. Plagioclase in contact with garnet coincides with particularly Ca-enriched rims on the garnet. b) X-ray maps taken from point 13 of the traverse, within polished thin section ps159. Low Ca content and lack of zonation in the garnet coincide with lower plagioclase (Pl) Ca content than at point 7. Muscovite (Ms), corundum (Crn) and K-feldspar (Kfs) are the other matrix minerals. Corundum as well as garnet has numerous inclusions of sillimanite.

(1998) and Chapman & Williams (1998), but the correlation of occurrences of grossular-rich garnet, pyroxene, pyroxenoids, and amphibole with those of Cl-rich biotite, K-feldspar, almandine and quartz veins and shears within the gneiss adds to the earlier interpretations through the identification of potential regionally extensive pathways for the fluid. The concentric nature of alteration around the Core Amphibolite may point to metasomatic interaction with the gneiss, but a previous investigator has not detected compositional gradients across the Core Amphibolite that might indicate fluid transfer (Smith 1999). Instead of homogeneous transfer of fluid between the amphibolite and gneiss, S_3 in the Core Amphibolite may have provided conduits for heterogeneous flow of fluid, resulting in compositional variation that is only detectable on the scale of the structures. There may have been metasomatic interaction between the Core Amphibolite and gneiss, but the amphibolite is not considered to be a major source of Fe and Ca for the development of the surrounding skarn. Event D_3 was the last one in which pyroxene + garnet was stable before the onset of hydrous retrograde metamorphism. Sulfide zonation around small bodies of amphibolite in the gneiss replicates the large-scale zonation surrounding the Core Amphibolite (Roache 2004), thus demonstrating the importance of D_3 metasomatism on the distribution of the sulfides.

CONCLUSIONS

Three phases of garnet growth correspond to three deformation events, D_1, D_2 and D_3, in the Southern Zone of the Cannington Ag–Pb–Zn deposit. The textural and compositional difference between D_3-related garnet and other assemblages from pre-existing phases enables a specific generation of altered gneiss to be genetically correlated with the formation of Ca–Mn silicate rocks. Infiltration coupled with hydrodynamic dispersion through D_3-related veins and shears was responsible for the formation of deposit-scale Ca–Mn silicate rocks. D_3-related biotite ± K-feldspar ± almandine ± quartz veins and shears may also transfer fluid, as deduced from veins filled with grossular-rich garnet, they extend beyond the deposit, and may be a regional indicator of a pathway for fluids that contributed to the formation of skarns. The distribution of retrograde mineralization replicates the distribution of Ca–Mn silicate rocks; therefore the joint mechanisms of deformation and metasomatism, particularly during D_3, were essential in the formation of the Cannington Ag–Pb–Zn deposit.

ACKNOWLEDGEMENTS

REFERENCES

BEARDSMORE, T.J., NEWBERY, S.P. & LAING, W.P. (1988): The Maronan Supergroup: an inferred early volcano-sedimentary rift sequence in the Mount Isa Inlier and its implications for ensialic rifting in the Middle Proterozoic of northwest Queensland. *Precamb. Res.* **40/41**, 487-507.

BELL, T.H. (1983): Thrusting and duplex formation at Mt Isa, Queensland, Australia. *Nature* **304**, 493-497.

BETTS, P.G., LISTER, G.S. & O'DEA, M.G. (1998): Asymmetric extension of the middle Proterozoic lithosphere, Mount Isa Terrane, Queensland, Australia. *Tectonophysics* **296**, 293-316.

BODON, S.B. (1998): Paragenetic relationships and their implications for ore genesis at the Cannington Ag–Pb–Zn deposit, Mount Isa Inlier, Queensland, Australia. *Econ. Geol.* **93**, 1463-1488.

BOWMAN, J.R., WILLETT, S.D. & COOK, S.J. (1994): Oxygen isotopic transport and exchange during fluid flow: one-dimensional models and applications. *Am. J. Sci.* **294**, 1-55.

CARMICHAEL, D.M. (1969): On the mechanism of prograde metamorphic reactions in quartz-bearing pelitic rocks. *Contrib. Mineral. Petrol.* **20**, 244-267.

CHAPMAN, L.H. (1993): *The Nature and Origin of Pyroxene – Amphibole – Garnet Alteration at the Cannington Deposit, NW Queensland*. Honours thesis, James Cook Univ. of North Queensland, Townsville, Australia.

_____ & WILLIAMS, P.J. (1998): Evolution of pyroxene – pyroxenoid – garnet alteration at the Cannington Ag–Pb–Zn Deposit, Cloncurry District, Queensland, Australia. *Econ. Geol.* **93**, 1390-1405.

CLECHENKO, C.C. & VALLEY, J.W. (2003): Oscillatory zoning in garnet from the Willsboro wollastonite skarn, Adirondack Mts, New York; a record of shallow hydrothermal processes preserved in a granulite facies terrane. *J. Metamorph. Geol.* **21**, 771-784.

EVANS, B.W. & GUIDOTTI, C.V. (1966): The sillimanite – potash feldspar isograd in western Maine, U.S.A. *Contrib. Mineral. Petrol.* **12**, 25-62.

FROST, B.R., MAVROGENES, J.A. & TOMKINS, A.G. (2002): Partial melting of sulfide ore deposits during medium- and high-grade metamorphism. *Can. Mineral.* **40**, 1-18.

GARCIA-CASCO, A., TORRES-ROLDÁN, R.L., MILLÁN, G., MONIÉ, P. & SCHNEIDER, J. (2002): Oscillatory zoning in eclogitic garnet and amphibole, Northern Serpentinite Melange, Cuba; a record of tectonic instability during subduction? *J. Metamorph. Geol.* **20**, 581-598.

GILES, D. (2000): *Tectonic Setting of Broken Hill-Type Mineralisation: the Cannington Perspective.* Ph.D. thesis, Monash Univ., Melbourne, Australia.

_____ & NUTMAN, A.P. (2002): SHRIMP U–Pb monazite dating of 1600–1580 Ma amphibolite facies metamorphism in the south-eastern Mt Isa Block, Australia. *Aust. J. Earth Sci.* **49**, 455-465.

_____ & _____ (2003): SHRIMP U–Pb zircon dating of the host rocks of the Cannington Ag–Pb–Zn deposit, southeastern Mt Isa Block, Australia. *Aust. J. Earth Sci.* **50**, 295-309.

GRANT, J.A. & WEIBLEN, P.W. (1971): Retrograde zoning in garnet near the second sillimanite isograd. *Am. J. Sci.* **270**, 281-296.

GRAY, D.R. (1992): *Structural Report on the Cannington Pb–Zn–Ag Deposit, Mount Isa Inlier.* Unpubl. Report to BHP Minerals.

HOLDAWAY, M.J. (2001): Recalibration of the GASP geobarometer in light of recent garnet and plagioclase activity models and versions of the garnet–biotite geothermometer. *Am. Mineral.* **86**, 1117-1129.

JAMTVEIT, B., WOGELIUS, R.A. & FRASER, D.G. (1993): Zonation patterns of skarn garnets: records of hydrothermal system evolution. *Geology* **21**, 113-116.

JEFFREY, S. (2002): The Cannington Ag–Pb–Zn BHT deposit; a world class discovery with a silver lining. *In* Geoscience 2002: Expanding Horizons, Abstracts of the 16th Australian Geological Convention (V.P. Preiss, ed.). *Geol. Soc. Aust.* **67**, 265.

KRETZ, R. (1983): Symbols for rock-forming minerals. *Am. Mineral.* **68**, 277-279.

KWAK, T.A.P. & TAN, T.H. (1981): The geochemistry of zoning in skarn minerals at the King Island (Dolphin) mine. *Econ. Geol.* **76**, 468-497.

LARSON, T.E. & SHARP, Z.D. (2003): Stable isotope constraints on the Al_2SiO_5 "triple-point" rocks from the Proterozoic Priest pluton contact aureole, New Mexico, USA. *J. Metamorph. Geol.* **21**, 785-798.

MARK, G. (1993): *Pegmatites and Partial Melting at the Cannington Ag–Pb–Zn Deposit.* Honours thesis, James Cook Univ. of North Queensland, Townsville, Australia.

_____, PHILLIPS, G.N. & POLLARD, P.J. (1998): Highly selective partial melting of pelitic gneiss at Cannington, Cloncurry District, Queensland. *Aust. J. Earth Sci.* **45**, 169-176.

PAGE, R.W. & SUN, S.-S. (1998): Aspects of geochronology and crustal evolution in the Eastern Fold Belt, Mt Isa Inlier. *Aust. J. Earth Sci.* **45**, 343-361.

POWELL, R., HOLLAND, T. & WORLEY, B. (1998): Calculating phase diagrams involving solid solutions via non-linear equations, with examples using THERMOCALC. *J. Metamorph. Geol.* **16**, 577-588.

RECHE, J. & MARTINEZ, F.J. (1996): GPT: an EXCEL spreadsheet for thermobarometric calculations in metapelitic rocks. *Comput. Geosci.* **22**, 775-784.

RICHMOND, J.M. (1994): *The Garnet – Quartz – Sillimanite Rich Envelope at the Cannington Ag–Pb–Zn Deposit, NW Queensland.* Honours thesis, James Cook Univ. of North Queensland, Townsville, Australia.

_____, CHAPMAN, L.H. & WILLIAMS, P.J. (1996): Two phases of garnet growth at the Cannington Ag–Pg–Zn deposit, NW Queensland. *In* New Developments in Metallogenic Research: the McArthur, Mt Isa, Cloncurry Minerals Province (T. Baker, J. Rotherham, J. Richmond, G. Mark & P. Williams, eds.). *James Cook University of North Queensland Economic Research Unit, Contrib.* **55**, 113-117.

ROACHE, T.J. (2004): Shear zone versus fold geometries at the Cannington Ag–Pb–Zn deposit: implications for the genesis of BHT deposits. *J. Struct. Geol.* **26**, 1215-1230.

ROCHE, M.T. (1994): The Cannington silver – lead – zinc deposit – at feasibility. *Aust. Inst. Mining Metall., Ann. Conf., Proc.*, 193-197.

SCHUMACHER, R., RÖTZLER, K. & MARESCH, W.V. (1999): Subtle oscillatory zoning in garnet from regional metamorphic phyllites and mica schists, western Erzgebirge, Germany. *Can. Mineral.* **37**, 381-403.

SMITH, M.J. (1999): *Geochemical and Paragenetic Characterization of the "Core Amphibolite", Cannington Ag, Pb, Zn Mine, Northwestern Queensland.* Honours thesis, James Cook Univ. of North Queensland, Townsville, Australia.

STOWELL, H.H., MENARD, T. & RIDGWAY, C.K. (1996): Ca-metasomatism and chemical zonation of garnet in contact-metamorphic aureoles, Juneau gold belt, southeastern Alaska. *Can. Mineral.* **34**, 1195-1209.

STRAIN, H. (1993): *Gold Mineralisation at the Cannington Ag–Pb–Zn Deposit, Northwest Queensland.* Honours thesis, James Cook Univ. of North Queensland, Townsville, Australia.

TODD, C.S. (1998): Limits on the precision of geobarometry at low grossular and anorthite content. *Am. Mineral.* **83**, 1161-1167.

VAUGHAN, J.P. & STANTON, R.L. (1986): Sedimentary and metamorphic factors in the development of the Pegmont stratiform Pb–Zn deposit, Queensland. *Trans. Inst. Mining Metall.* **95**, B94-121.

VERNON, R.H. (1979): Formation of late sillimanite by hydrogen metasomatism (base-leaching) in some high-grade gneisses. *Lithos* **12**, 143-152.

WALTERS, S.G. (1998): Broken Hill-type deposits. *AGSO J. Aust. Geol. Geophys.* **17**, 229-237.

_____ & BAILEY, A. (1998): Geology and mineralisation of the Cannington Ag–Pb–Zn Deposit: an example of Broken Hill-type mineralisation in the Eastern Succession, Mount Isa Inlier, Australia. *Econ. Geol.* **93**, 1307-1329.

WILLIAMS, P.J., DONG GUOYI, PRENDERGAST, K., POLLARD, P.J. & RYAN, C.G. (1999): Metasomatism and metal mobility in Broken Hill-type deposits. *In* Mineral Deposits: Processes to Processing (C.J. Stanley *et al*. eds.). Balkema, Rotterdam, The Netherlands (999-1002).

_____ & PHILLIPS, G.N. (1992): Cloncurry mapping project 1990: Geology of the Selwyn Range (McKinlay River and Maramungee Creek areas). *James Cook University of North Queensland Economic Research Unit, Contrib.* **40**, 1-21.

WILLNER, A.P., HERVÉ, F. & MASSONNE, H.-J. (2000): Mineral chemistry and pressure–temperature evolution of two contrasting high-pressure – low-temperature belts in the Chonos Archipelago, southern Chile. *J. Petrol.* **41**, 309-330.

YANG, PANSEOK & RIVERS, T. (2001): Chromium and manganese zoning in pelitic garnet and kyanite; spiral, overprint, and oscillatory (?) zoning patterns and the role of growth rate. *J. Metamorph. Geol.* **19**, 455-474.